ELSEVIER

Contents lists available at ScienceDirect

# Mechanics of Materials

journal homepage: www.elsevier.com/locate/mechmat



# Research paper



# Impact and adhesion mechanics of block copolymer micro-particles with a silicon substrate

Salih Duran<sup>a</sup>, Ara Kim<sup>b</sup>, Jae-Hwang Lee<sup>b,c</sup>, Sinan Müftü<sup>a,\*</sup>

- <sup>a</sup> Department of Mechanical and Industrial Engineering, Northeastern University, Boston, MA, 02115, USA
- <sup>b</sup> Department of Mechanical and Industrial Engineering, University of Massachusetts, Amherst, MA, 01003, USA
- <sup>c</sup> Materials Science and Engineering Graduate Program, University of Massachusetts, Amherst, MA, 01003, USA

# ARTICLE INFO

#### Keywords: Ultra-high strain rate Cold spray Polymer PS-b-PDMS LIPIT

# ABSTRACT

Deformation of a two-phase block copolymer (BCP) during high velocity impacts is studied experimentally and theoretically with an aim to use this material in cold spray (CS) additive manufacturing. Micron scale ( $10-20~\mu m$ ) spherical particles of polystyrene-block-polydimethylsiloxane (PS-b-PDMS) are impacted on a silicon substrate by using a laser-induced projectile impact test (LIPIT) setup with impact velocities in the range of 50-600~m/s. Experiments indicate that polymer particles adhere to the substrate when their impact velocities fall within the range of 140-500~m/s. A constitutive model that accounts for the effects of both strain rate and temperature on the mechanical behavior of such materials is developed. A critical energy release rate function which depends on the surface temperature and rate of separation is formulated and used in a cohesive zone model (CZM) to model bonding of the BCPs on the substrate. The model parameters are calibrated by comparing the deformed and computed deformed particle shapes and coefficient of restitution values of the rebounding particles. Simulations show that the particles experience ultra-high strain rates ( $>10^4~s^{-1}$ ), large deformation, and temperature elevation due to plastic dissipation and interfacial friction. The outer rim of the contact interface is predicted to experience temperature levels above the glass transition temperature of the PS-domain of the BCP. Bonding is correlated with increase of contact area, plastic dissipation and temperature rise in the interface.

# 1. Introduction

Cold particle gas spray, which is simply known as a cold spray (CS), is an additive manufacturing technology where powdered material particles are consolidated into functional coatings and/or near net shape parts by using high energy impacts (Van Steenkiste et al., 1999; Moridi et al., 2014; Stoltenhoff et al., 2002; Papyrin et al., 2007). The particles are mixed with a compressible gas and are accelerated in a converging-diverging de Laval nozzle to high-impact velocities (Van Steenkiste et al., 1999; Moridi et al., 2014; Stoltenhoff et al., 2002; Papyrin et al., 2007). Upon impact, most of the kinetic energy in the particles is dissipated in plastic work, and the particles can bond onto a substrate or onto one another depending on the balance between the bonding, elastic rebound, and plastic dissipation energies. In fact, particle-to-substrate and particle-to-particle bonding are related but two distinct processes (Sabard and Hussain, 2019). CS additive manufacturing (AM) has been successfully demonstrated with ductile metal particles and has found a niche in repair of high value components (Barnett, 2012). In metal CS applications, the particles remain well below their melting temperatures (Moridi et al., 2014; Grujicic et al., 2003). Therefore, the resulting coatings can retain the properties of the powdered material in its nascent state, and experience lower residual stresses as compared to other AM processes that rely on phase change (i. e., melting) for particle-to-particle bonding (Smith, 2007). The native oxide layer on metal particles plays and important role in the bonding and metallurgical bonding has been demonstrated to take place between cold sprayed metal particles (Flanagan et al., 2019; Evans et al., 2019).

Polymer coatings are generally used for providing corrosion protection, heat stability, wear resistance, mechanical strength, and biocompatibility (Kausar, 2018). Cold spray of polymers is an emerging research area with relatively small number of journal articles published to date, despite its potential applications. Among the polymers that have been cold sprayed are high- and low-density polyethylene (H/LDPE), ultra-high molecular weight polyethylene (UHMWPE), polystyrene (PS), and polyamide (PA) (Xu and Hutchings, 2006; Bush et al., 2017; Alhulaifi et al., 2012; Khalkhali and Rothstein, 2020; Ravi et al., 2015). Xu

E-mail address: s.muftu@northeastern.edu (S. Müftü).

<sup>\*</sup> Corresponding author.

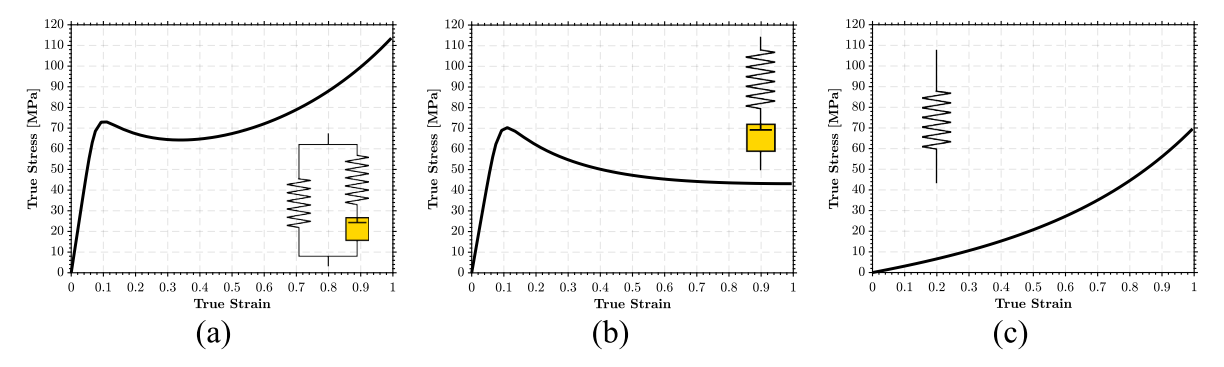


Fig. 1. Stress-strain response of a) overall resistance b) elastic-viscoplastic resistance c) hyperelastic resistance.

and Hutchings successfully deposited 150-250 µm diameter HDPE particles onto HDPE substrates (Xu and Hutchings, 2006). Bush et al. deposited HDPE particles onto HDPE, LDPE, Al-6061, and quartz substrates. Alhulaifi et al. deposited 65  $\mu m$  diameter HDPE particles onto aluminum substrates (Bush et al., 2017). Ravi et al. deposited UHMWPE onto aluminum substrates. They investigated the effect of mixing alumina nanoparticles with polymer particles on the deposition efficiency (DE) and reported DE of up to 10% (Ravi et al., 2015). Khalkhali and Rothstein, 2020 and Ravi et al., 2015 showed that using a polymer with low glass transition temperature  $(T_g)$  is more conducive to achieving deposits with higher levels of DE. Khalkhali et al. also reported the successful deposition of PS and PA powders onto PS, PA, and LDPE substrates with less than 5% DE (Khalkhali and Rothstein, 2020). Anni et al., 2023 presented a study on the feasibility of cold spray coating of nylon 6 on fiber-reinforced composite substrates. By varying process parameters, DE of over 30% has been achieved without causing significant damage to the substrate. Muthulingam et al., 2023 investigated the deposition of glassy thermoplastics using cold spray, and achieved uniform polymer coatings without the need for solvents or high temperatures. The results suggest that plastic deformation, shear induced interfacial bonding, molecular-weight-dependent fracture of the sprayed glassy polymers affect the deposition process, especially when spraying soft thermoplastics on hard substrates. Molecular weight is a critical variable in the cold spray of glassy polymers, and understanding the interplay between plastic yielding and fracture can optimize the material-process relations for improved polymer cold spray processing conditions.

In general, successful particle deposition in CS depends on several process parameters, including particle impact velocity, particle and substrate temperatures, and nozzle-to-substrate distance among others (Xu and Hutchings, 2006; Bush et al., 2017; Alhulaifi et al., 2012; Khalkhali and Rothstein, 2020; Ravi et al., 2015; Shah et al., 2017; Khalkhali et al., 2018). These variables can be indirectly controlled by the cold spray gas temperature, pressure, and nozzle geometry. Both for metal and polymer cold spray, a window of impact velocities exists below which no deposition takes place and above which the impacts cause excessive material damage (Khalkhali and Rothstein, 2020; Khalkhali et al., 2018). The deposition window is specified by the lower and upper critical impact velocities,  $V_{c1}$  and  $V_{c2}$ , respectively. Experimental work cited above has shown that  $V_{c1}$  is on the order of 100 m/s for polymers and the deposition window changes with the process parameters, powder, and substrate material (Khalkhali and Rothstein, 2020; Khalkhali et al., 2018).

Block copolymers (BCPs) such as polystyrene-block-poly-dimethylsiloxane (PS-b-PDMS) can contain alternating segments of different homopolymer compositions, resulting in a phase-separated morphology that consists of glassy and rubbery domains due to thermodynamic incompatibility (Jung and Ross, 2007). However, it is important to note that the type of domains formed in BCPs can also depend on the glass transition temperature ( $T_g$ ) of each polymer. It is possible for BCPs to consist entirely of glassy domains or entirely of

rubbery domains, depending on the  $T_g$  of each individual polymer. At room temperature, the soft phase (e.g. PDMS) could be above its glass transition temperature ( $T_g$ ) and show rubbery state behavior, whereas the hard phase (e.g. PS) could be below its  $T_g$  and exhibit glassy state behavior. Mechanical performance of BCPs depends on the properties and weight percentage of the individual polymer domains (Veysset et al., 2017; Lee et al., 2012). Copolymers show dynamic stiffening and strengthening mechanisms, which enhance their ability to absorb and dissipate energy (Veysset et al., 2017; Sun et al., 2019; Wu et al., 2019; Grujicic et al., 2013; Hyon et al., 2018). BCPs' ability to absorb and dissipate energy by the their phases makes them favorable for use in high strain rate deformation events such as impact and blast loadings (Veysset et al., 2017) as well as in CS additive manufacturing (Khalkhali et al., 2018).

The research and development of the CS process has been carried out experimentally, computationally, and theoretically (Xu and Hutchings, 2006; Bush et al., 2017; Alhulaifi et al., 2012; Khalkhali and Rothstein, 2020; Shah et al., 2017; Khalkhali et al., 2018; Che et al., 2019; Ozdemir et al., 2019, 2021; Hassani-Gangaraj et al., 2018; Schmidt et al., 2009; Rokni et al., 2019; Bortolussi et al., 2020; Ganesan et al., 2013). Well-developed computational models save time and resources and provide a deep understanding of the intrinsic material behavior in transient processes (Che et al., 2019; Chen et al., 2018; Lin et al., 2019; Xie et al., 2017; Schreiber et al., 2021). High-strain rate (HSR,  $10^3$  -  $10^4$ s<sup>-1</sup>) material behavior for ductile metals is typically represented by phenomenological models such as the Johnson-Cook or physically based models such as the Preston-Tonks and Wallace (PTW) models, among others (Muthulingam et al., 2023; Che et al., 2019; Chen et al., 2018; Lin et al., 2019; Xie et al., 2017; Schreiber et al., 2021). Particle impacts in CS typically experience strain rate higher than  $10^4$  s<sup>-1</sup>. The material behavior for ductile metals in this ultra high strain rate (UHSR) regime can be modeled by phenomenological and physically based models (Xie et al., 2017; Armstrong and Zerilli, 1994; Gao and Zhang, 2012; J.G., 1983; Preston et al., 2003; Voyiadjis and Abed, 2005; Tuazon et al., 2014; Chakrabarty and Song, 2020; Couque et al., 2006; Othman, 2015; Al-Juaid and Othman, 2016; El-Qoubaa and Othman, 2015; Lesuer et al., 2001; Manes et al., 2013; Manes et al., 2011). Using ductile metal plasticity flow models for polymers may not be suitable as the deformation mechanisms between metals and polymers are significantly different.

Developing and calibrating constitutive material models that cover the strain rates and temperatures in CS manufacturing processes and modeling the cohesive interaction between particles and the substrate is necessary to investigate the impact behavior of polymers accurately. The goal of this work is to investigate the material behavior during impact of the PS-b-PDMS and identify the conditions that lead to bonding. To this end, single-particle impact experiments are performed; a strain rate and temperature-dependent constitutive model for this BCP is developed, calibrated, and validated. Mechanics of the acceleration and impact phases of the particle are simulated by using large deformation continuum mechanics. Material model parameters were tuned by minimizing

the error between the experimentally observed and numerically computed coefficients of restitution and the global deformation ratio of the particles. The bonding window was investigated by using a cohesive zone model, and the material behavior during high strain rate impact was revealed.

#### 2. Constitutive model

A typical BCP with rubbery- and glassy-domains has the following characteristic response mechanisms under increasing compressive loading: i) nonlinear elastic response with a nonlinear elastic-plastic transition; ii) exponential softening, and; iii) exponential hardening (Fig. 1). Cho et al. introduced a microstructurally informed threedimensional constitutive model for copolymer polyurea (Cho et al., 2017). Their model considered elastic-viscoplastic (Fig. 1a) and hyperelastic deformation (Fig. 1b) mechanisms as two deformation pathways working concurrently. These two mechanisms contribute to the overall Cauchy stress tensor independently. Therefore, the overall stress tensor can be calculated by the direct superposition of the two branches. In this work, the general framework provided by Cho et al. (2017) was used to define a new physically based, empirically tuned constitutive model for the UHSR deformation of PS-b-PDMS. To this end the constitutive equations for each microstructural part of the rheological model have been modified as described below.

# 2.1. Kinematics of the proposed model

The material model has two distinct deformation mechanisms as intermolecular or elastic-viscoplastic resistance (I) and network or hyperelastic resistance (N). According to the rheological model depicted in Fig. 1, the deformation gradient is identical in the two branches,

$$\mathbf{F} = \mathbf{F}_{\mathbf{I}} = \mathbf{F}_{\mathbf{N}} \tag{1}$$

Volume change of each part is expressed by the determinant of the deformation gradient,

$$J_{\rm I} = J_{\rm N} = \det \mathbf{F} \tag{2}$$

The left-Cauchy-Green strain tensor is defined as follows:

$$\mathbf{b} = \mathbf{F}\mathbf{F}^{\mathsf{T}} \tag{3}$$

We assume that limiting stretch dominates the hardening behavior of PS-b-PDMS as in many copolymer systems. Therefore, the Arruda-Boyce eight-chain model was used to capture the *hyperelastic stretching* and *rotation in the polymer*. Thus, the Cauchy stress for the eight-chain model (Arruda and Boyce, 1993) is expressed as follows:

$$\sigma_{N} = \frac{\mu_{N}}{J\overline{\lambda}^{*}} \frac{\mathscr{L}^{-1}\left(\frac{\overline{\lambda}^{*}}{\lambda_{L}^{N}}\right)}{\mathscr{L}^{-1}\left(\frac{1}{\lambda_{L}^{N}}\right)} dev\left[\mathbf{b}_{N}^{*}\right] + \kappa_{N}(J-1)\mathbf{I}$$
(4)

where  $\mu$  and  $\kappa$  are the shear and bulk moduli, respectively, J is the volumetric change based on the deformation gradient,  $\lambda_L$  is the limiting chain stretch,  $\mathbf{b}_N^* = J^{-2/3}\mathbf{b}_N$  is the distortional left Cauchy-Green tensor,  $\overline{\lambda^*} = (\text{tr}[\mathbf{b}_N^*]/3)^{1/2}$  is the applied chain stretch, **I** is the identity tensor, and  $\mathscr{L}^{-1}$  is the inverse Langevin function (Bergström and Boyce, 2000).

Constitutive modeling of *elastic-viscoplastic resistance* contains a flow component that helps to capture nonlinear elastic-plastic transition and softening behavior. The Cauchy stress is expressed as follows (Bergström, 2022):

$$\sigma_{I} = \frac{\mu_{I}}{J^{e}\overline{\lambda}^{e*}} \frac{\mathscr{L}^{-1}\left(\frac{\overline{\lambda}^{e*}}{\overline{\lambda}_{I}^{I}}\right)}{\mathscr{L}^{-1}\left(\frac{1}{\overline{\lambda}_{I}^{I}}\right)} dev\left[\mathbf{b}_{I}^{e*}\right] + \kappa_{I}(J^{e} - 1)\mathbf{I}$$
(5)

where  $J^e=\det{[F_I^e]}$ ,  $\mu$  is the initial shear modulus,  $\lambda_L^I$  is the chain locking strech,  $\mathbf{b}_I^{e*}=(J_I^e)^{-2/3}F_I^eF_I^{eT}$ , is the Cauchy-Green deformation tensor,  $\overline{\lambda^{e*}}=(tr[\mathbf{b}_I^{e*}]/3)^{1/2}$  is the effective chain stretch. Power-law model was used to predict effective deviatoric flow rate as follows (Bergström, 2022):

$$\dot{\gamma}^p = \left(\frac{\tau}{f_{pp}f_0\hat{\tau}}\right)^m \tag{6}$$

where  $\dot{\gamma}^p$  is the effective deviatoric flow rate,  $\tau$  is the effective stress,  $\hat{\tau}$  is the shear flow resistance,  $f_{\theta}$  models the temperature dependency,  $f_{\varepsilon^p}$  models the yield evolution of the flow model, and m is the shear flow exponent. The yield evolution factor is given by the following relationship (Bergström, 2022):

$$f_{\varepsilon^p} = \frac{1}{2} \sum_{i=1}^{2} \left[ f_i + (1 - f_i) exp\left( -\frac{\varepsilon_p}{e_i} \right) \right]$$
 (7)

where  $f_i$  and  $e_i$  are empirically determined constants, and  $\varepsilon_p$  is the von Mises plastic strain,

$$\varepsilon_p = \sqrt{\frac{2}{9} \left[ \left( \varepsilon_1^{\nu} - \varepsilon_2^{\nu} \right)^2 + \left( \varepsilon_2^{\nu} - \varepsilon_3^{\nu} \right)^2 + \left( \varepsilon_3^{\nu} - \varepsilon_1^{\nu} \right)^2 \right]}$$
 (8)

where  $\varepsilon_i^{\nu}$  are the components of the inelastic principal strain.

The temperature factor is formulated with the following relationship (Bergström, 2022):

$$f_{\theta} = 1 + q \frac{\theta - \theta_0}{\theta_0} \tag{9}$$

where q is the temperature scaling factor and  $\theta_0$  is the reference temperature taken as the room temperature (293 K).

Equations (5)–(9) describe the constitutive behavior for *elastic-vis-coplastic resistance*, and Equation (4) describes the constitutive behavior for *hyperelastic resistance*. The constitutive behavior for the BCP is obtained by superposition of the two components,

$$\sigma = \sigma_I + \sigma_N \tag{10}$$

where  $\sigma_I$  and  $\sigma_N$  are the Cauchy stresses of the elastic-viscoplastic part and hyperelastic respectively and  $\sigma$  is the overall Cauchy stress of the system. The constitutive model presented above was constructed by using a commercially available polymer material modeling library, PolyUMod (ver. 6.3.4, PolymerFEM, Needham, MA) (Bergström, 2022).

Since polymer particles have low thermal diffusivity  $(10^{-7} \text{ m}^2/\text{s})$ , the HSR deformation can be considered adiabatic. Therefore, a significant portion of the work done on the material is transformed into heat and causes temperature rise. The temperature rise can be determined from the energy balance between the inelastic work and heat storage capacity of the system,

$$\Delta T = \frac{\beta}{\rho C_p} \int \sigma \, d\varepsilon_p \tag{11}$$

where  $\rho$  is the mass density and  $C_p$  is the specific heat of the material,  $d\varepsilon_p$  is the plastic strain increment. The integral in equation (11) represents the inelastic work. Taylor-Quinney coefficient ( $\beta$ ) is an empirically determined constant with values in the range of 0.8–1 for polymers at high strain rates (Shao et al., 2017; Kendall et al., 2014).

# 2.2. Validation of the constitutive model

The constitutive model described above has eleven empirical parameters that need to be determined. To evaluate its effectiveness, we tested this model for polyurethane, another block copolymer with glassy- and rubbery-domains, for which experimental data exists in the HSR range (Cho et al., 2017). The HSR response of a polymer is largely

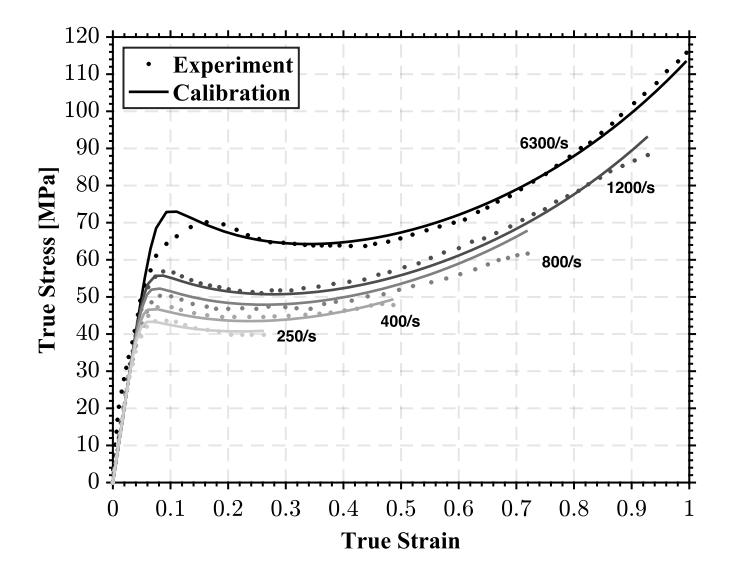


**Fig. 2.** Validation of the constitutive model using experimental test results of polyurethane compression adapted from Sarva et al. (Sarva et al., 2007). Data is reproduced with permission.

governed by its mechanical properties, such as its elastic modulus, yield initiation, yield evolution and finite strain chain responses which are influenced by factors such as the polymer's molecular weight, chain architecture, and glass transition temperature. Since both polyurethane and PS-b-PDMS share similarities in their molecular structures and physical properties, we expect that they will show similar HSR responses. A similar assumption was made by Cho et al., who developed a constitutive model for a thermoplastic block copolymer by using experimental results for polyurethane (Cho et al., 2017). Experimental data in reference (Sarva et al., 2007) for polyurethane was used to determine the parameters of the constitutive model presented above. A commercially available material calibration software MCalibration (ver.

6.5.5, PolymerFEM, Needham, MA) was used for this purpose. Fig. 2 shows uniaxial compression test results for polyurethane obtained by using a split Hopkinson pressure bar at strain rates ranging from 250 to  $6300 \, {\rm s}^{-1}$  (Sarva et al., 2007). It is seen that the model described above is very effective in capturing the characteristic features of the multiphase thermoplastic deformation in medium  $(1\text{-}10^3 \, {\rm s}^{-1})$  to high strain rate (HSR)  $(10^3\text{-}10^4 \, {\rm s}^{-1})$  regimes. This constitutive model is extended to the ultra high strain rate (UHSR)  $(>10^4 \, {\rm s}^{-1})$  regime, and a method to determine the model parameters by using micro-particle impact experiments is presented in this paper.

# 2.3. Cohesive zone model

Adhesion between the particle and the substrate is modeled by using the traction-separation based *cohesive zone model* (CZM) (Lin et al., 2019; Xie et al., 2017; Needleman, 1990; Yildirim et al., 2015). The traction-separation approach tracks the effective separation distance between two surfaces and follows defined constitutive relations. The traction-separation law is approximated as a nonlinear relationship, as shown in Fig. 3. Separation values in the range of  $0 \le \delta \le \delta_c$  are elastically recoverable. The elastic response of the cohesive zone is modeled with an elastic constitutive matrix that relates the normal and shear tractions ( $\hat{t}$ ) of the interface to its normal and shear separations  $\delta$  as follows:

$$\bar{\mathbf{t}} = \mathbf{K}\boldsymbol{\delta} \tag{12}$$

where K is the cohesive stiffness matrix,  $\bar{t} = \{\bar{t}_1\bar{t}_2\bar{t}_3\}^T$  with  $\bar{t}_1$ ,  $\bar{t}_2$  and  $\bar{t}_3$  as the traction values in 1, 2, and 3 directions of crack opening and  $\delta = \{\delta_1\delta_2\delta_3\}^T$  with  $\delta_1$ ,  $\delta_2$  and  $\delta_3$  as the crack opening displacements. The area under the traction-separation curve represents the *critical strain energy release rate* ( $G_c$ ).

In one-dimensional problems, damage propagation is initiated if the separation distance between the two surfaces exceeds the *critical separation distance*. In three-dimensional problems, damage propagation is initiated when a suitable damage criterion is reached. In this work, the

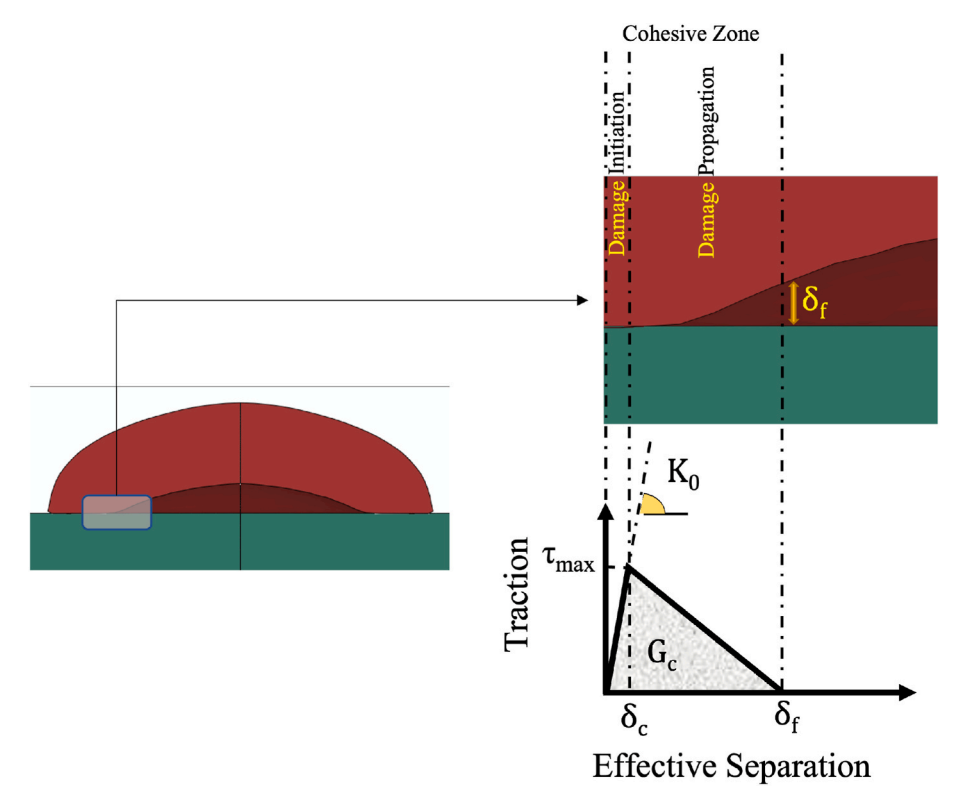


Fig. 3. Schematic representation of cohesive zone model – finite element model correlation.

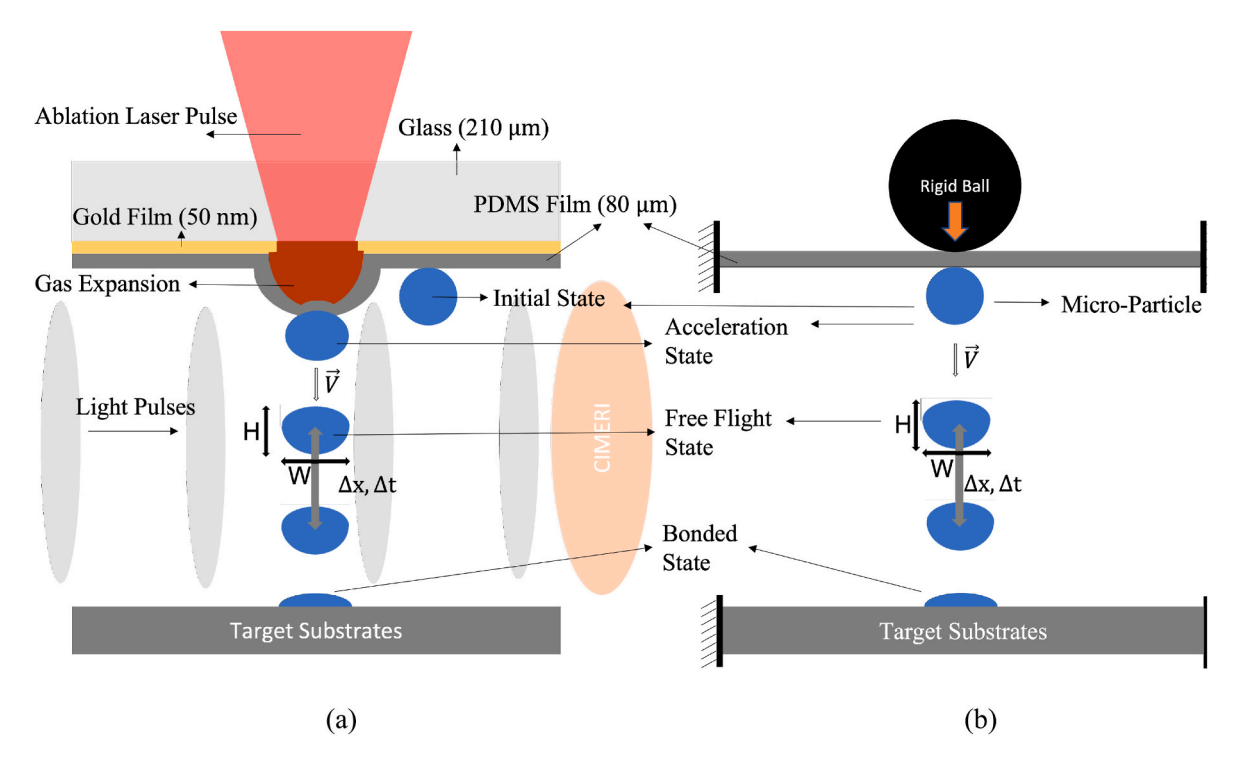


Fig. 4. (A) Schematic description of the α-LIPIT experiment setup. (b) Schematic description of the ABAQUS/Explicit simulations. Acceleration, free-flight, and impact-and-rebound phases of the experiment are simulated in a single connected sequence of simulations.

quadratic traction criterion, which is defined as follows, is used:

$$\left(\frac{\langle \bar{t}_1 \rangle}{t_1^o}\right)^2 + \left(\frac{\bar{t}_2}{t_2^o}\right)^2 + \left(\frac{\bar{t}_3}{t_2^o}\right)^2 = 1 \tag{13}$$

where  $t_1^o, t_2^o$  and  $t_3^o$  are the limiting values for interlaminar traction in each direction. The  $\langle . \rangle$  symbol represents the Macaulay bracket which yields zero traction for compressive loads. In three-dimensional problems, the damage evolution phase starts if equation (13) is satisfied.

Damage evolution under combined loading depends on the *effective* separation distance,

$$\delta_m = \sqrt{\langle \delta_n \rangle^2 + \delta_s^2} \tag{14}$$

where  $\delta_n$  and  $\delta_s$  are the magnitudes of effective separation in normal and shear directions, respectively. In the damage evolution phase, a scalar damage variable, D, controls the degradation of the adhesive strength,

$$D = \frac{\delta_m^f \left(\delta_m^{max} - \delta_m^o\right)}{\delta_m^{max} \left(\delta_m^f - \delta_m^o\right)} \tag{15}$$

where  $\delta_m^f$ , and  $\delta_m^o$  represent the effective separation at complete failure, and at damage initiation, respectively, and  $\delta_m^{max}$  is the maximum effective separation value during loading. D starts from zero and increases monotonically to one. During this phase, the traction components are updated with the current value of D as follows,

$$t_1 = \begin{cases} (1-D)\overline{t}_1, \overline{t}_n \ge 0\\ \overline{t}_1, \text{ otherwise} \end{cases}$$
 (16)

$$t_2 = (1 - D)\bar{t}_2 \tag{17}$$

$$t_3 = (1 - D)\overline{t}_3 \tag{18}$$

where  $\bar{t}_1, \bar{t}_2, \bar{t}_3$  are the traction components computed by equation (12) without any damage.

In general, the critical strain energy release rate of bonded joints

depends on the temperature  $T_s$  and rate of separation  $\dot{\delta}$  of the two surfaces  $G_c = G_c(T_s, \dot{\delta})$  (Banea et al., 2012; Feng et al., 2023; Marzi et al., 2009). In this work, a functional relationship between  $G_c$  and  $T_s$ , and  $\dot{\delta}$  values was determined after  $G_c$  values were found, as described later in the paper. As a first order of approximation, the following linear relationship is adopted in this work:

$$G_c(T_s, \dot{\delta}) = c_1 + c_2 T_s + c_3 \dot{\delta} \tag{19}$$

where  $c_1 - c_3$  are empirically determined coefficients.

## 2.4. Frictional energy dissipation model

Frictional dissipation energy refers to the work done to overcome the frictional forces when two objects in contact experience relative tangential motion. Most of this frictional dissipation energy is converted to heat, which increases the *contact temperature* at the point of contact. The contact temperature is a combination of the bulk temperature (the average temperature of the entire body), the ambient temperature (the temperature of the surrounding environment), and the flash temperature (a local temperature over the area of contact). Although the flash temperature has a short lifetime ( $10^{-3}$  s or less (Blok, 1963)), it is important for cold spray particle impacts, which last for less than 50 ns. The heat flux due to frictional sliding can be calculated as follows:

$$q = \eta \tau \frac{\Delta s}{\Delta t} \tag{20}$$

where q is the frictional heat flux per unit area,  $\eta$  is the fraction of frictional energy converted to heat (assumed as 1),  $\tau(=\mu p)$  is the shear stress due to friction with  $\mu$  as the friction coefficient, p as the contact pressure.  $\Delta s$  is the incremental slip, and  $\Delta t$  is the time increment. In this work we assume that the frictional heat flux is partitioned equally and instantly between two sliding bodies.

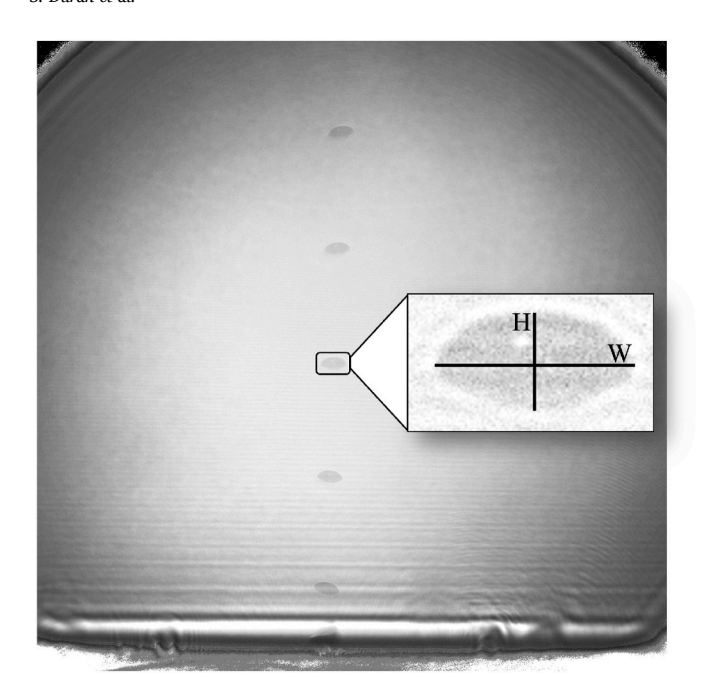
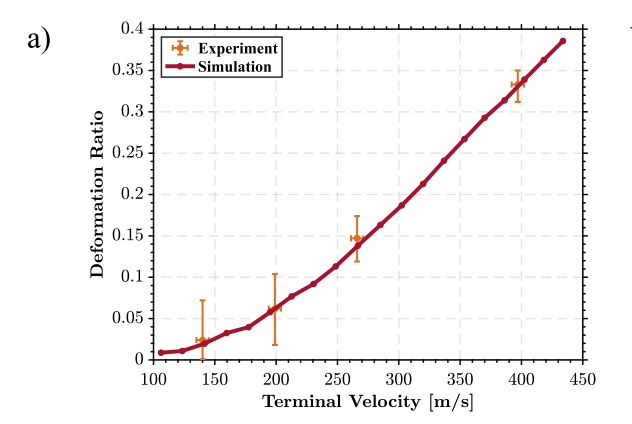


**Fig. 5.** Sequence of particle images captured with 138 ns time intervals for  $V_i = 451 \, m/s$ . Close inspection of the particles during in the free-flight phase shows that they have experienced considerable deformation before they impact the substrate.

## 3. Experiments

# 3.1. Laser-induced particle impact test

To investigate the material behavior under UHSR conditions, an advanced *laser-induced particle impact test* ( $\alpha$ -LIPIT) setup (Fig. 4) was used (Lee et al., 2012). In this setup the particle launching pad consists of a microscope cover glass coated with gold and cross-linked PDMS membrane. A microparticle is placed on the PDMS layer. The gold layer, ablated by a single laser pulse, evaporates and rapidly, causing localized expansion of the PDMS membrane. The expanding PDMS membrane in turn accelerates the particle. Particles velocities well over  $10^3$  m/s can be achieved with this method. The particle is illuminated during the experiment by ultrafast pulses (Fig. 4a) and recorded by a high frame-rate camera. The individual exposures thus correspond to consecutive probe pulses with a pre-defined time interval. It can be shown that air drag on the particle is negligible. Post-processing of the images reveals morphological material behavior before and after impact, as well as the impact and rebound velocities.



BCP-particles that consist of PS-*b*-PDMS with diameters in the range of  $10-20~\mu m$  were manufactured with equal molecular weight composition (82.5 kg/mol-82.5 kg/mol) of the constituent polymers. The particles were subsequently annealed at  $120~^{\circ}C$  for 24 h. Nevertheless, the experiments were conducted with both annealed and unannealed microparticles, and no noticeable difference in the results were observed. Impact experiments were performed by using the  $\alpha$ -LIPIT setup with impact velocities in the range of 80-600~m/s.

#### 3.2. Experimental results

The particle images captured during flight (Fig. 5) show that the particles can be considerably deformed before they hit the substrate. We quantify this deformation by using the *deformation ratio* ( $R_D$ ),

$$R_D = 1 - \frac{H}{W} \tag{21}$$

where H and W are the height and width of the particle in the terminal velocity state. Fig. 6a shows the measured deformation ratio as a function of the impact velocity ( $v_i$ ) of the particle. This ratio starts from zero for undeformed particles and increases to 0.33  $\pm$  0.02 at the terminal velocity value of 400  $\pm$  5 m/s.

The rebound energy of the particles is characterized by the *coefficient* of restitution,

$$e = \frac{v_r}{v_i} \tag{22}$$

where  $v_r$  and  $v_i$  are the rebound and impact velocities of the particle. Fig. 6b shows the measured coefficient of restitution as a function of the impact velocity. The scatter in these results is attributed to particle shapes and short standoff distance. Some of the particles are not perfectly spherical and have flat regions induced during the annealing process. These irregularly shaped particles could gain spin and tangential velocity components during the acceleration phase potentially resulting in the observed scatter. Another cause for the scatter is attributed to the internal velocity gradients that the soft particles experience during the free flight phase. The particles sustain significant internal energy which involves elastic strain energy, and inelastic dissipation energy, during the flight due to their relatively low stiffness, which could contribute to the scatter.

The coefficient restitution plot (Fig. 6b) shows three distinct regions (I–III) for the particles' rebound characteristics. In region-I, e decreases with increasing impact velocity. This decrease is attributed to the increasing levels of plastic dissipation in the particle (Manes et al., 2011). Region-II represents the *bonding window* which spans the impact velocities of  $\sim$ 140 $-\sim$ 500 m/s. The velocity at the lower limit of this window is known as the *critical velocity of bonding* (Yildirim et al., 2015).

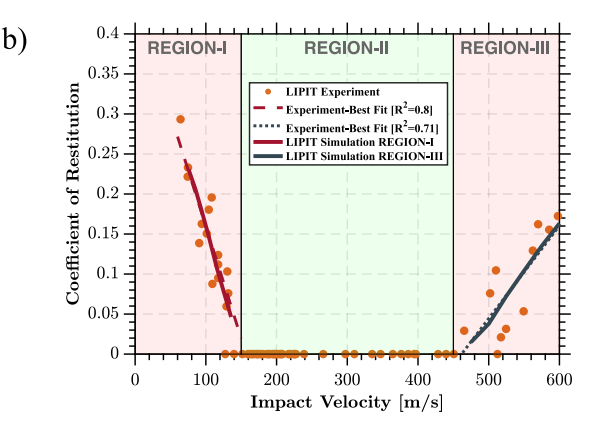


Fig. 6. Comparison between simulation and experimental results a) for deformation ratio after acceleration in the free-flight phase, and b) for the coefficient of restitution e after impact.

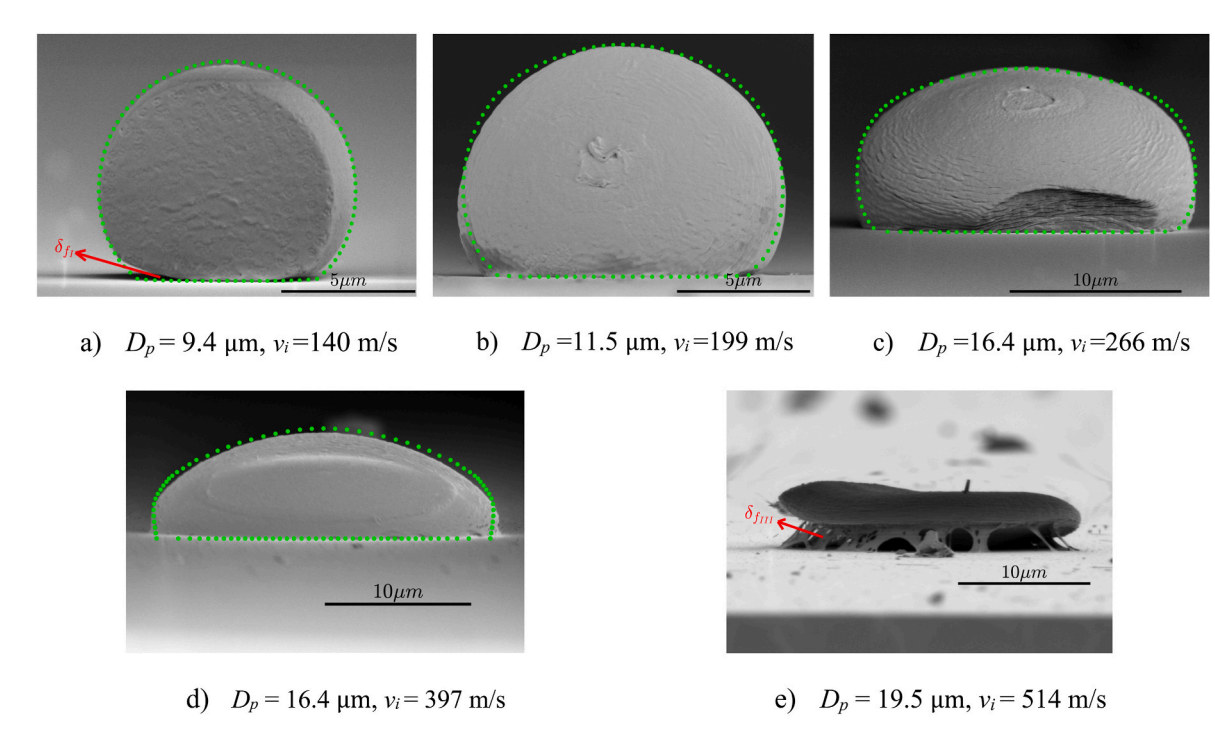


Fig. 7. SEM images of the particles and the simulation results (middle cross section) indicated by scattered green dots for a) 140 m/s, b) 199 m/s, c) 266 m/s, and d) 397 m/s. These cases (a–d) were used for material calibration. e) SEM image of a partially delaminated particle with an impact velocity of 514 m/s, is showcased to illustrate the change in bonding mechanics. (For interpretation of the references to colour in this figure legend, the reader is referred to the Web version of this article.)

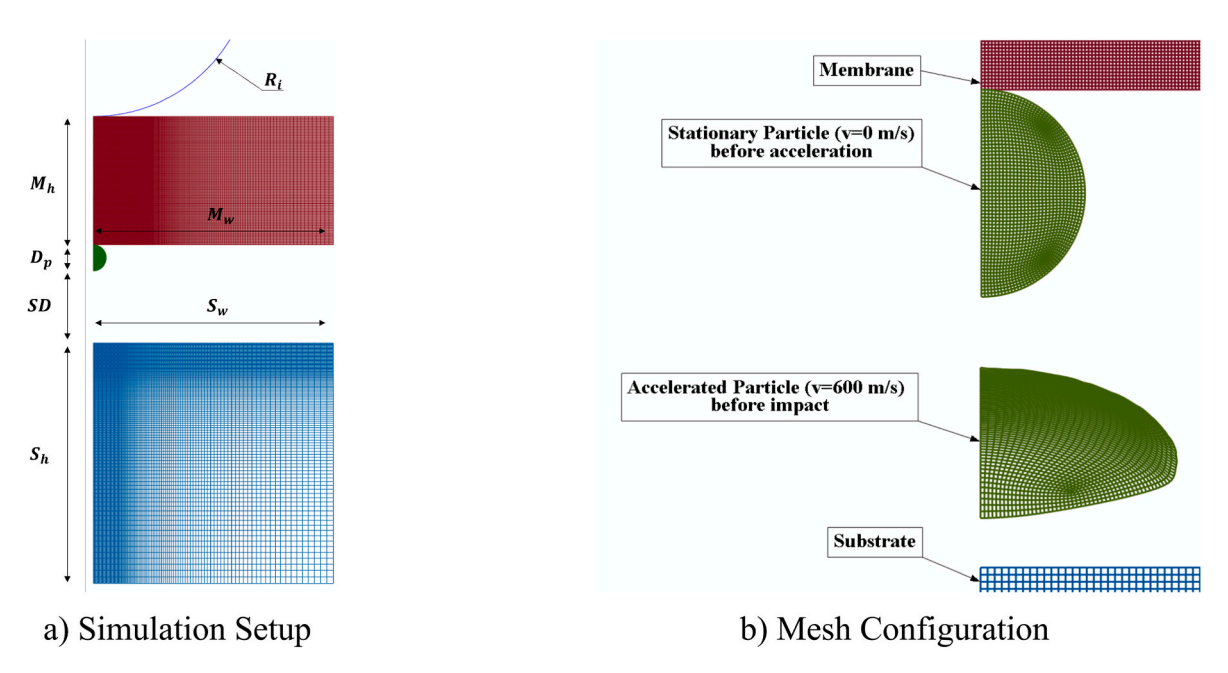


Fig. 8. A) Simulation setup with dimension abbreviations, b) mesh configuration of initial state and before impact state for  $v_i = 600 \text{ m/s}$ .

In region-III, *e* increases with impact velocity. This increase is attributed to the excessive kinetic energy of impact that causes the bonds to be broken (Manes et al., 2011).

Scanning electrone microscope (SEM) images of the bonded particles are shown in Fig. 7. Particles experience increasing levels of deformation and flattening with impact velocity increasing from 140 m/s to 514 m/s. The particle that hit the surface with 514 m/s of impact velocity experienced extreme flattening and physics beyond what is included in the model, such as cohesive failure, formation of filaments, and most likely melting. This case also illustrated the changing bonding mechanism

from adhesion-effective region (I), where the bond strength is lower than the material strength, to a combined adhesion and cohesion-effective region (III), where the bond strength exceeds the material strength. Therefore, Fig. 7e was not used for material calibration or validation.

# 4. Numerical simulations

The experiments show that the deformation history of the material in the  $\alpha$ -LIPIT experiment consists of three sequential phases: *acceleration*,

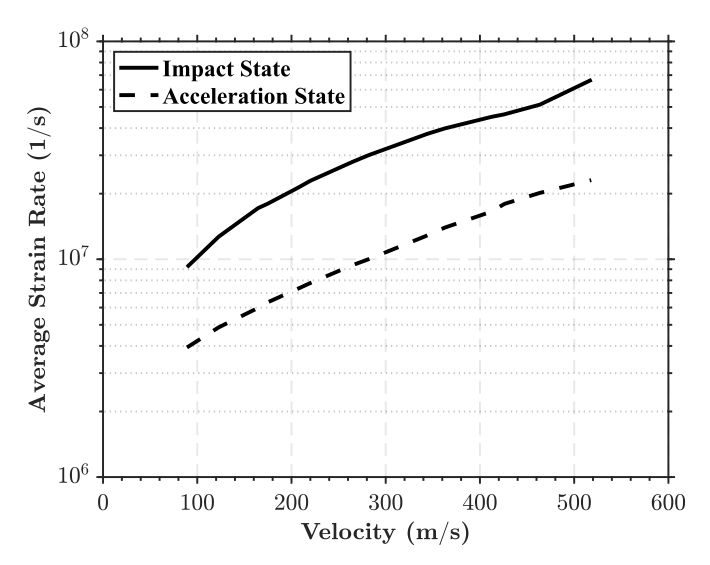
**Table 1** Simulation parameters.

Membrane (cross-linked PDMS)			
Constitutive model	Arruda-Boyce Model		
Dimensions, $M_{h_i}$ $M_w$	80, 1000 μm		
Density, ρ	0.97 g/cm <sup>3</sup>		
Shear modulus, μ	2.5 MPa		
Bulk modulus, k	100 MPa		
Limiting chain stretch, $\lambda_1$	1.28		
Substrate (Silicon Wafer)			
Constitutive model	Linear Elastic		
Dimensions, $S_{h_i}$ $S_{w}$	500, 500 μm		
Density, ρ	2.2 g/cm <sup>3</sup>		
Elastic modulus, E	73.1 GPa		
Poisson's ratio, v	0.17		
Particle (PS-b-PDMS)			
Constitutive model	VUMAT-PolyUMod		
Dimension, $D_p$	16.4 μm		
Other			
Stand Off Distance, SD	860 μm		
Radius of Rigid Ball, $R_i$	100 μm		

**Table 2**Calibrated material parameters for PS-*b*-PDMS.

		Elastic-Viscoplastic Resistance	Hyperelastic Resistance
Shear modulus [MPa]	μ	1148	4.2
Locking stretch	$\lambda_L$	4.59	2.8
Bulk modulus*[MPa] (Cho et al., 2013)	κ	2845	246
Shear flow resistance [MPa]	$\widetilde{ au}$	15.43	_
Shear flow exponent	m	5.29	_
Parameter for $f_{\varepsilon^p}$	$f_1$	$6  imes 10^{-5}$	-
Parameter for $f_{\varepsilon^p}$	$e_1$	0.13	_
Parameter for $f_{\varepsilon^p}$	$f_2$	2.2	_
Parameter for $f_{\varepsilon^p}$	$e_2$	2.8	_
Temperature dependence of the $\dot{\gamma}^p$	q	-0.62	-

\*The bulk modulus for each network was calculated with formulation for homogenous isotropic material assumption, and poisson's ratio is taken 0.33 for Elastic-Viscoplastic Resistance and 0.49 for Hyperelastic Resistance.



 $\begin{tabular}{lll} Fig. & {\bf 9.} & {\bf Average} & {\bf strain} & {\bf rate} & {\bf of} & {\bf the} & {\bf particle} & {\bf during} & {\bf acceleration} & {\bf and} \\ & {\bf impact} & {\bf phases}. & & & \\ \end{tabular}$ 

free-flight, and impact-and-rebound. These phases were simulated successively in order to represent the deformation history of the material accurately. Commercially available finite element software package

Abaqus/Explicit, v. 2020 (Dassault System, Pawtucket, RI, USA) was used together with the PolyUMod software. The schematic representation of the simulation setup is illustrated in Fig. 4b, while its finite element model is shown in Fig. 8. The initially stationary particle was accelerated by the sudden expansion of the PDMS membrane. The constitutive model for the PDMS membrane is the hyperelastic eightchain Arruda-Boyce model (Arruda and Boyce, 1993), whose parameters are given in Table 1.

Membrane expansion was initiated by using a rigid ball impact on the opposite side of the membrane instead of simulating the gold ablation. Desired terminal velocity of the particle was obtained by tuning the impact velocity of the rigid ball. In the experimental setup, a silicon wafer was used as the substrate. No permanent deformation was observed on the wafer due to particle impacts throughout the experiment. Therefore, the substrate was modeled as linear-elastic material (Table 1). Axisymmetric geometry was used in the simulations. The membrane and the substrate were partitioned into volumes with progressively denser mesh sizes near the contact regions to reduce the computational cost. Membrane and substrate dimensions were chosen such that waves reflected from the far-boundaries do not have enough time to reach the regions of interest during the interaction. For calibration of the properties of the constitutive model, the specific particle size of each experiment was used for each simulation. For calibration of the cohesive zone model, the average particle size of 16.4  $\mu m$  from the experiments was used. The calibration of the PS-b-PDMS material properties is described in the next section.

The microparticles were discretized by using the CAX4RT element with size of  $D_p/60$ , and the membrane and the substrate were meshed by using the CAX4R element. Both of these are four node, linear interpolation elements. The CAX4RT element has temperature and displacement degrees of freedom, whereas the CAX4R has only displacement degrees of freedom. Reduced integration and enhanced hourglass control were used for both element types. Contact between the particlemembrane and particle-substrate surfaces was modeled by using the general contact algorithm with tangential-penalty and normal-hard contact characteristics. In addition, the cohesive zone model (CZM) described earlier was defined to model the bonding between the particle and the substrate.

### 4.1. Calibration of model properties

Parameters of the constitutive model for the PS-b-PDMS and parameters of the CZM were determined by using an iterative optimization method. The optimization was performed by using the commercially available software tool MCalibration (ver. 6.3, PolymerFEM, Needham, MA) along with Abaqus/Explicit. These parameters were calibrated by minimizing the error between the measured and computed deformation ratios  $R_D$  for the free-flight and post-impact phases, shown in Figs. 6a and 7, respectively. Once the material properties were determined, the CZM calibration was done by minimizing the error between the best-fitof experimental results and the computed coefficient of restitution e values (Fig. 6b). Note that the CZM model was calibrated for region-I and region-III, because only in these two regions the entire magnitude of the bonding energy  $G_c$  has been depleted. In region-II, where the experiments showed bonding, we used a perfect bonding approach in computations and determined a bonding energy that must have been in the interface based on the total energy balance of the system. This is explained further in Section 5.2.

At each iteration, except for the first cycle, numerical simulation results were processed by using Python programming language and delivered to MCalibration for calculation of the correction values. Normalized mean absolute difference (NMAD) is used as the error metric,

$$\epsilon_{NMAD} = \frac{\langle |y - p| \rangle}{\max(\langle |y| \rangle, \langle |p| \rangle)}$$
 (23)

**Table 3**Critical fracture toughness parameters  $G_c$  for the separation rate and temperature-dependent model of Equation (18).  $R^2$  indicates goodness of fit and p indicates statistically significant of the correlation, p-value of 0.05 or lower is generally considered statistically significant correlation.

	$T_s(K)$	$\dot{\delta}(\frac{m}{s})$	$c_1(-)$	$c_2\left(\frac{kg}{s^2 \times K}\right)$	$c_3\left(\frac{kg}{m\times s}\right)$	$R^2$	p
Region-I	298 - 304	1.9 - 2.2	-81	0.292	0.702	0.995	0.0044
Region-III	356 - 381	56 - 66	-251.7	-1.23	13.22	0.992	0.0079

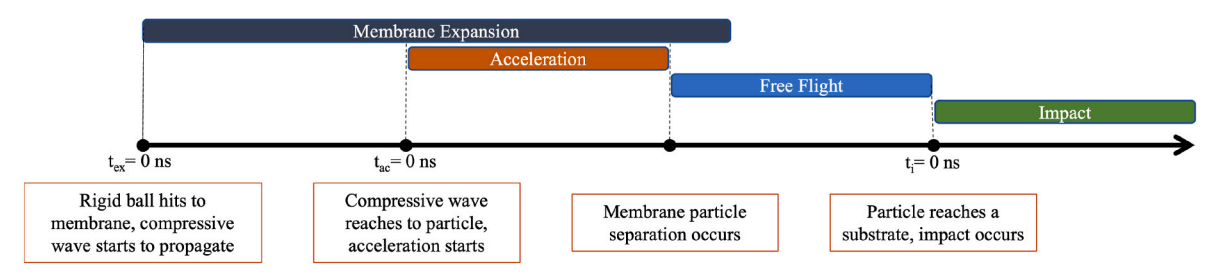


Fig. 10. Summary of distinct timelines used in this study. Evaluations of membrane expansion are stoped during free flight stage of the particle.

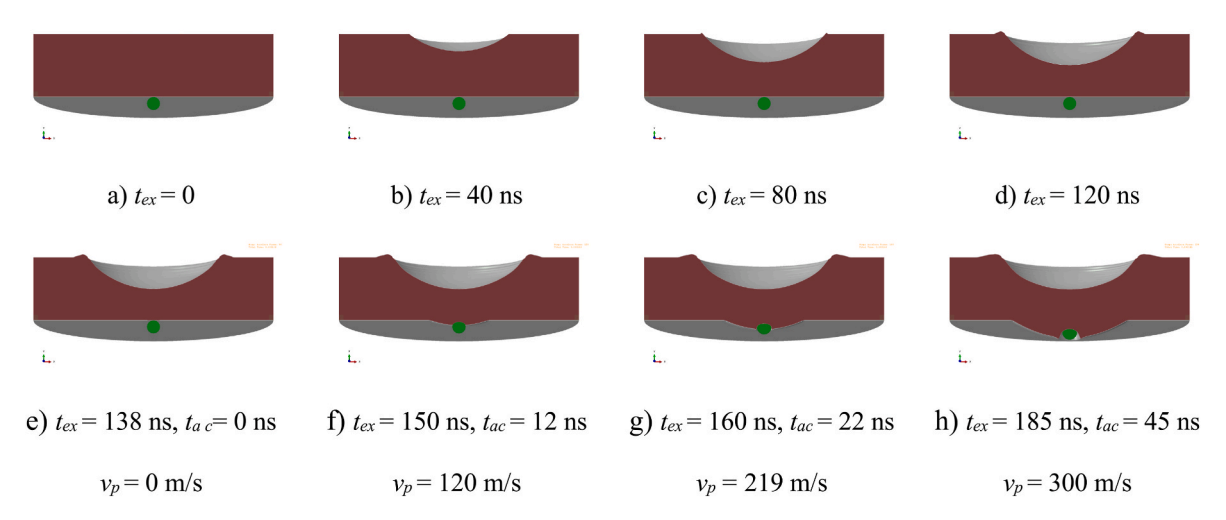


Fig. 11. Evaluation of membrane expansion and its interaction with the particle. Details of the particle membrane interaction can be observed in.

where y is a vector containing one of measured  $R_D$  or e values and p is a vector containing one of computed  $R_D$  or e values depending on the parameter being optimized. Eleven material model parameters  $\{\mu_1, \lambda_{L1}, \mu_2, \lambda_{L2}, q, \widehat{r}, m, f_1, f_2, e_1, e_2\}$  were thus determined.

# 5. Results and Discussion

Material parameters obtained for PS-b-PDMS are reported in Table 2. Experimental and numerical model results presented in Figs. 6 and 7 have a good agreement, as it should be expected after a concerted fitting process. Thus, using impact experiments via LIPIT looks promising to determine the material properties for UHSR deformation for an appropriate constitutive model. The average strain rate in the particle was computed during acceleration and impact by averaging each integration point of the particle. Fig. 9 illustrates the variation of strain rate with velocity of the particle during acceleration and impact stages. The average strain rate varies between  $0.3 \times 10^6 \, \text{s}^{-1}$  and  $2 \times 10^7 \, \text{s}^{-1}$  in the acceleration stage and 2  $\times$  10  $^7$  s  $^{-1}$  and 7  $\times$  10  $^7$  s  $^{-1}$  in the impact stage for terminal velocities that are in the range of 80-514 m/s. Favorable comparison of the measured and simulated results presented in Figs. 6 and 7 indicate that the material model proposed for the BCP in this work, gives acceptable results for strain rates that are on the order of 10<sup>5</sup>–10<sup>8</sup>  $s^{-1}$ .

In the second step of the optimization, the CZM parameters were

optimized by using the same method. Six different target e values in regions-I and –III were selected and calibrated for  $G_c$  to match the experimental results shown in Fig. 6b. The terminal separation distance  $\delta_f$  was set to 0.54 µm for region-I and 2.86 µm for region-III. These values are approximated based on the experimental results and shown with a red arrow and labeled as  $\delta_{fi}$  and  $\delta_{fm}$  in Fig. 7a for region-I and Fig. 7e for region-III, respectively. Maximum adhesion stress  $(\tau_{\rm max})$ ) is then calculated based on  $G_c$  and  $\delta_f$ . For instance, for the  $G_c = 9.3 \, {\rm J/m^2}$ , in region-I, since  $\delta_f$  was set to 0.54 µm,  $\tau_{max}$  was calculated as 34.4 MPa. To fully define the CZM, the damage initiation ratio  $(\delta_c/\delta_f)$  is taken as 0.5 for both region-I and region-III. Therefore the only independent parameter in the CZM definition is the critical strain energy release rate  $G_c$ . A similar approach to determine CZM parameters was used by Diehl, 2008a, 2008b.

After the calibration of  $G_c$  values, a correlation study was conducted, and strong relation was found between  $G_c$ , and  $T_s$  and  $\dot{\delta}$  values. This relationship and the parameters of the critical strain energy release rate model given in Equation (18) are presented in Table 3. This model accurately captures the deposition window of the PS-b-PDMS, as shown in Fig. 6b, which yields  $G_c = 9.3 \text{ J/m}^2$  at the low end of the bonding window and  $G_c = 48 \text{ J/m}^2$  at the high end.

The modeling framework presented above allows the investigation of plastic deformation and temperature generation in UHSR impact events. The evolution of these parameters cannot be observed experimentally in

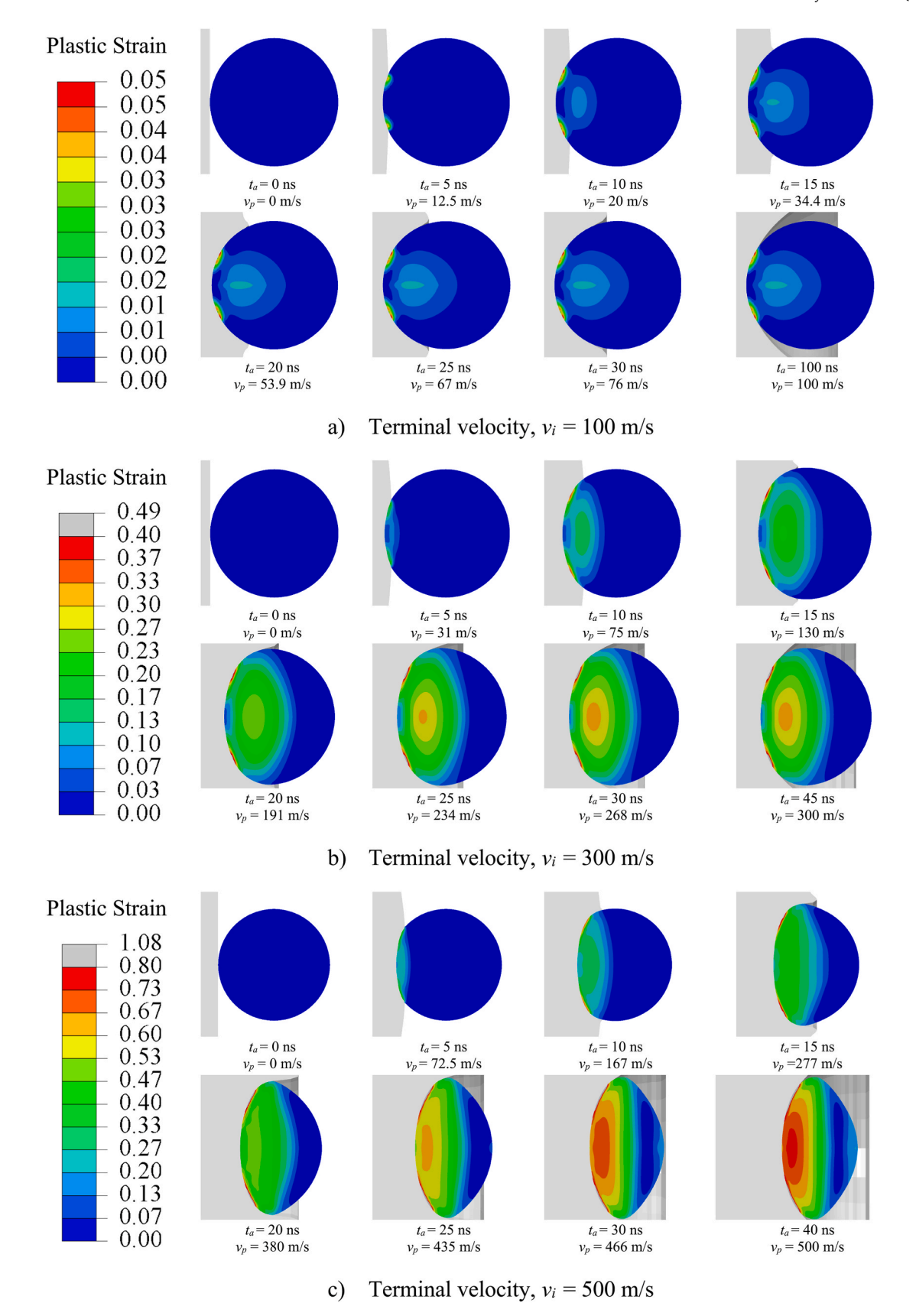


Fig. 12. Effective plastic strain evolution during acceleration of the particle for terminal velocity of a) 100 m/s b) 300 m/s c) 500 m/s.

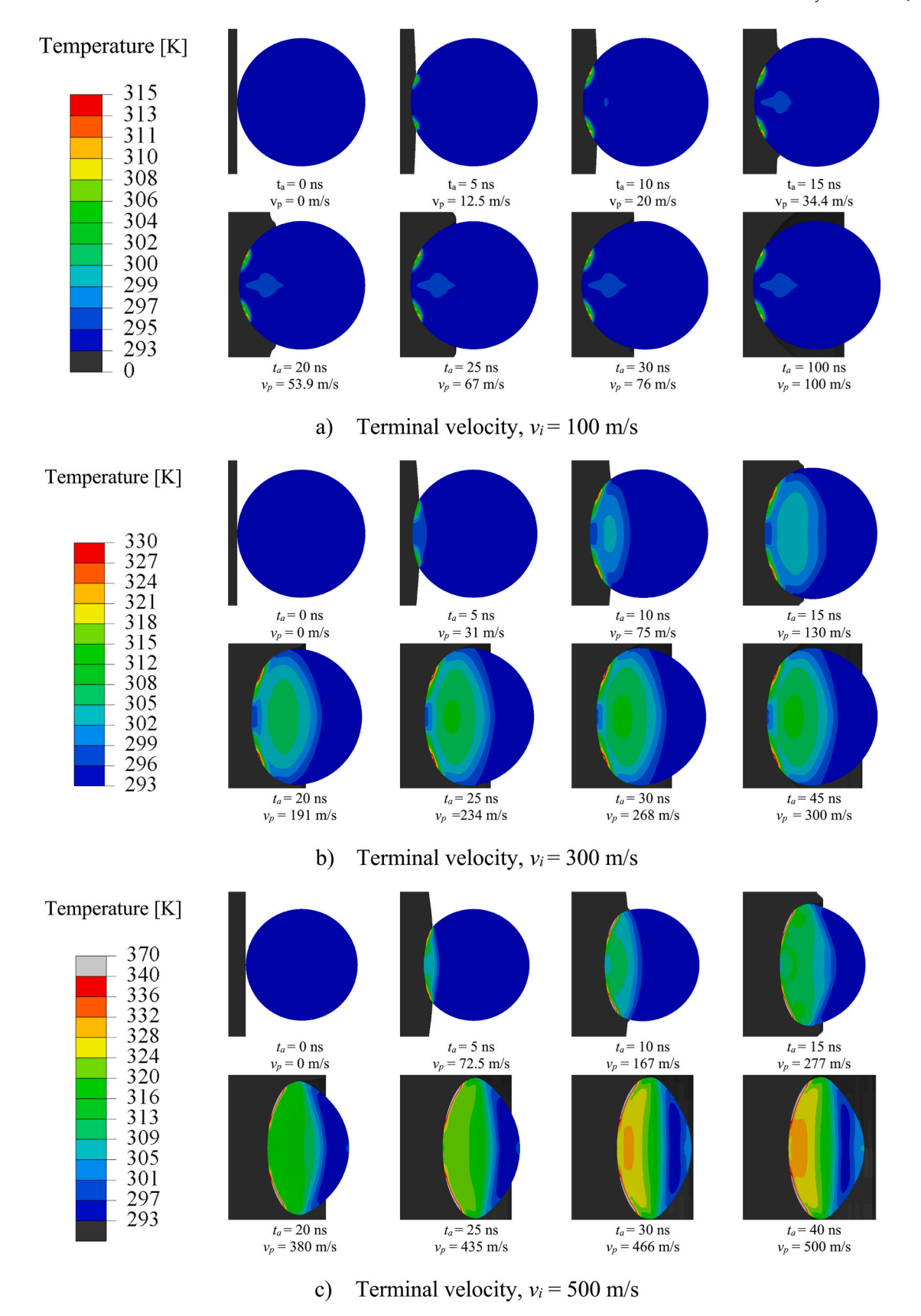


Fig. 13. Temperature evolution during acceleration of the particle for terminal velocity of a) 100 m/s b) 300 m/s c) 500 m/s.

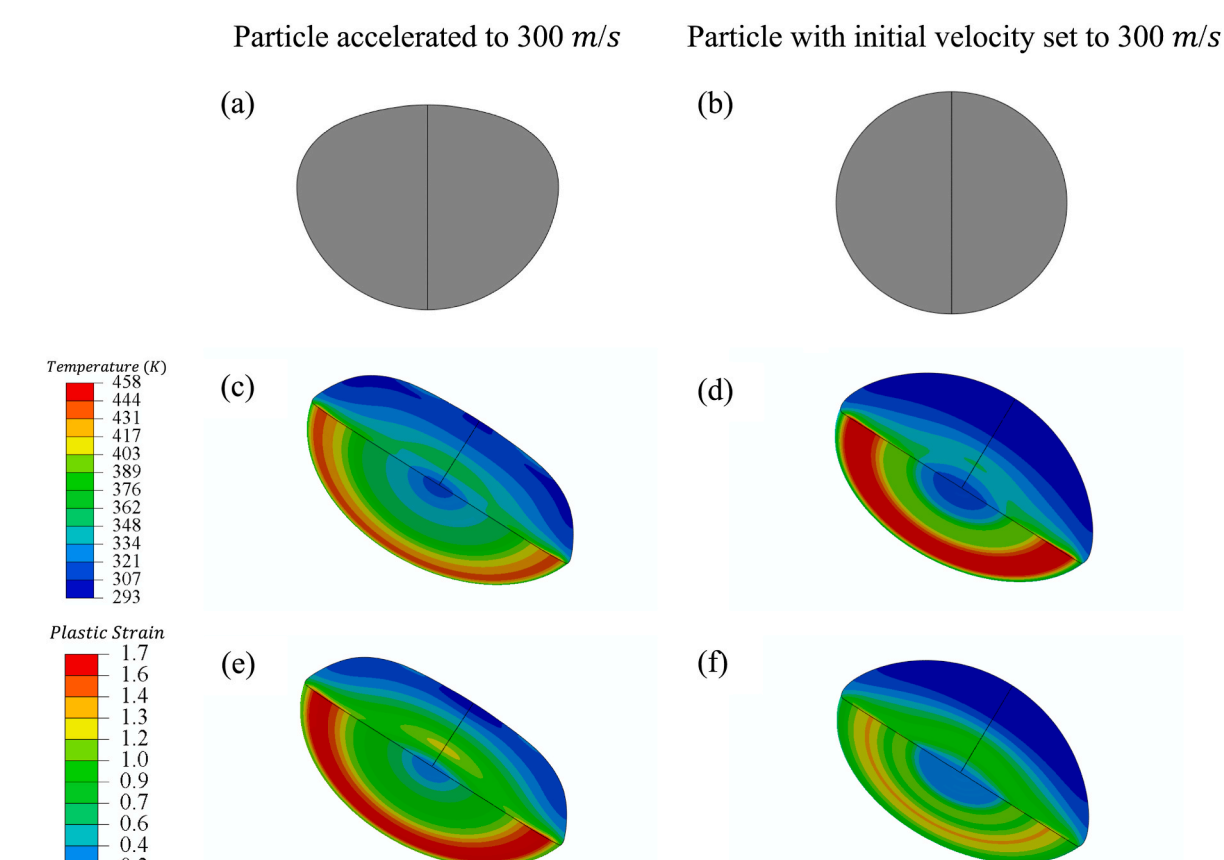


Fig. 14. Influence of acceleration-induced effects on the temperature and plastic strain profiles after impact. Figures (a), (c) and (e) show the shape of the particle before impact, and the temperature, and plastic strain distributions after impact, respectively, for a particle accelerated using the LIPIT simulation (described in Fig. 4b) to 300 m/s. Figures (b), (d), and (f) show the same for an undeformed spherical particle with the initial velocity of 300 m/s.

transient events such as cold spray applications. Next, we give a detailed account of plastic deformation and temperature rise during the acceleration and impact phases for  $v_i = 100$ , 300, and 500 m/s. Note that the terms *terminal velocity* and *impact velocity* are used interchangeably, and both are indicated by the symbol  $v_i$ . Three distinct timelines were used in the following:  $t_{ex}$  represents the *membrane expansion timeline* and starts when the rigid-ball hits the membrane starting a the compressive wave;  $t_{ac}$  represents the *particle acceleration timeline* and starts when compressive wave inside the membrane reaches the particle and particle starts to accelerate;  $t_i$  represents the *particle impact timeline* which starts when the particle impacts the substrate (Fig. 10).

## 5.1. Acceleration-phase

In the experimental setup (Fig. 4a), the PDMS membrane expands when the gold layer behind it suddenly evaporates in response to laser ablation. Sudden expansion of the membrane causes the particle to accelerate to a terminal velocity,  $v_i$ . In simulating this chain of events, the compression waves created by the expanding gas of gold were simulated by impacting a rigid-ball on the back side of the membrane, as shown in Fig. 4b. Thus the terminal velocity of the particle was controlled by adjusting the velocity of the rigid-ball. Fig. 11 shows a sequence of frames for  $v_i = 300$  m/s, starting with the moment when the ball reaches the membrane ( $t_{ex} = 0$ ), followed by the propagating compressive wave reaching the particle ( $t_{ac} = 0$ ), followed by the acceleration of the particle lasting until the membrane and the particle separate ( $t_{ex} = 185$  ns,  $t_{ac} = 45$  ns), eventually resulting in the terminal velocity of 300 m/s. The compressive wave initiated on the ball-impact side of the membrane reaches the front of the membrane in 138 ns. Once

the compressive wave reaches the front face of the membrane it starts to expand laterally while being slightly impeded by the particle. The particle-membrane interaction results in the membrane wrapping itself around the particle, thus increasing the contact area while imparting forward momentum to the particle. The particle eventually separates from the membrane at  $t_{ac}=45$  ns with the terminal velocity,  $v_i=300$  m/s

Details of the plastic strain and temperature in the particle during the acceleration phase are presented in Figs. 12 and 13, respectively. Fig. 12 shows the deformation and equivalent plastic strain histories for  $v_i$ values of 100, 300, and 500 m/s. As expected, more energy is transferred through the membrane by increasing the impact velocity of the rigid ball, which in turn causes more severe permanent deformation in the particle and faster terminal velocity. These figures show that along the way to reach the terminal velocities of 100, 300, and 500 m/s, the particles develop maximum plastic strain values of 0.05, 0.49, and 1.08, respectively. Temperature evolution during the acceleration phase is presented in Fig. 13. In general, friction and plastic dissipation are the two sources of temperature generation. The maximum change of temperature at the moment when the particle separates from the membrane is 22 K for terminal velocity of 100 m/s and 77 K for 500 m/s. Two dissipation mechanisms can be observed distinctly in the 300 m/s case where the temperature rise around the contact interface is primarily dominated by frictional sliding, whereas the temperature increase inside the particle is dominated by plastic action in the material where higher internal stresses are expected. However, these two effects merge for faster  $v_i$  values. .

One can question the influence of acceleration-mechanism provided by the LIPIT setup on the mechanics of the particles. To investigate this

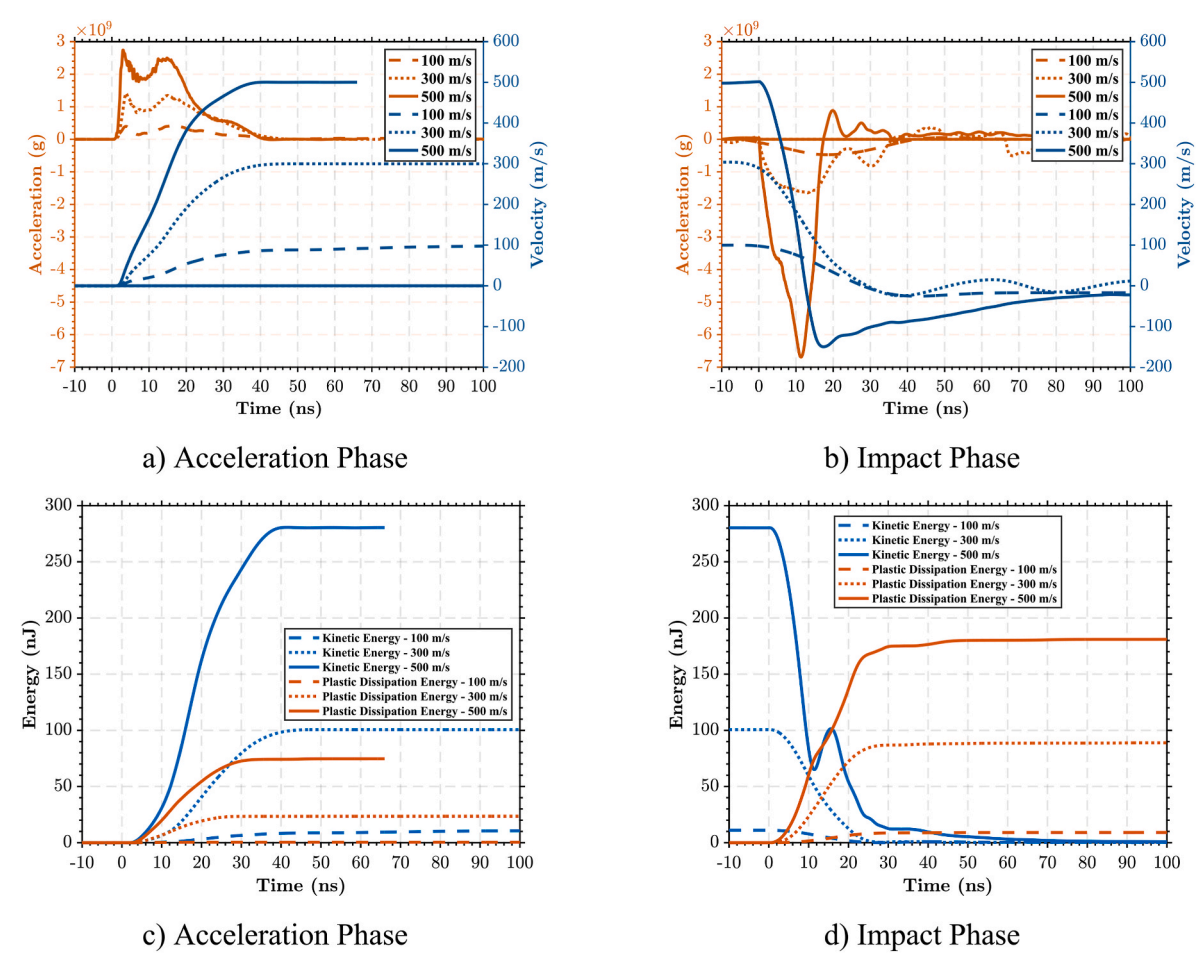


Fig. 15. Acceleration and velocity profile during a) acceleration and b) impact phases, plastic strain, and kinetic energy evolution during c) acceleration and d) impact phases of the particle for terminal velocity of 100 m/s 300 m/s, 500 m/s.

effect, the impact of a particle accelerated by the LIPIT setup and the impact of an undeformed spherical particle are compared at the terminal impact velocity of 300 m/s in Fig. 14. In the latter case, the particle has a perfect spherical morphology, shown in Fig. 14b, and it is in a stress and strain-free state. On the other hand, the accelerated particle shows a deformed morphology and has a non-zero strain state before impact at  $t_i = 0$ . Details of this strain state are presented later in the paper.

Fig. 14(c) and (d) show that the spherical particle experiences higher temperatures in the contact interface after contact. This is attributed to more frictional dissipation/heating due to the longer sliding distance experienced by the spherical particle during contact. The equivalent plastic strain distributions in the particles after contact are shown in Fig. 14(e) and (f). The particle accelerated by the LIPIT system has a higher accumulated plastic strain due to its prior deformation history. The differences in the interfacial temperatures and equivalent plastic strain change the overall energy balance of the system.

The influence of acceleration-induced changes on impact and adhesion mechanics, as detailed in Fig. 14, leads us to explore the acceleration phase further. Details of this phase are quantified by using the average velocity and acceleration in Fig. 15a. Two peaks are observed in the acceleration phase. The first peak is dominated by the energy transferred by the front of the compression wave, and the second peak is dominated by the energy transferred due to the momentum of the membrane. The acceleration peaks nearly in the first 5 ns after the initial expansion wave hits the particle and reaches  $0.2-2.9 \times 10^9 \, \mathrm{g.}^1$  The

duration of the acceleration phase is approximately 40 ns for all three cases, after which the particle separates from the membrane and the terminal velocity is reached. Fig. 15c shows the kinetic energy of the particle and plastic energy dissipation during the acceleration phase. Comparing the evolution of acceleration with that of energy dissipation (Fig. 15a and c) shows that most of the energy is dissipated during the rise of acceleration, where the first derivative is greater than zero. Friction-induced energy dissipation (not shown in the figures), which is around 0.5 nJ in all three impact velocities, is considerably lower than the plastic energy dissipation except for  $v_i = 100$  m/s. Frictional dissipation is localized on the contact interface, and it is the primary source for temperature increase at the contact interface, as shown in Fig. 13. Energy dissipation due to plastic action is the only source of temperature increase inside the particle. The level of plastic dissipation at the moment of separation of the particle from the membrane is approximately 0.4, 23.4, and 74.6 nJ, for  $V_i = 100$ , 300, and 500 m/s, respectively. After the acceleration, particles experience free flight, Comparing the state of the particle at the end of the acceleration phase with their state just before impact shows that particles do not experience any changes during the free flight. This observation aligns with experimental results, which indicate no shape change during the free flight, as shown in Fig. 5.

# 5.2. Impact-phase and bonding

The temporal evolution of the equivalent plastic strain and temperature during the impact phase are presented in Figs. 16 and 17, respectively. In this phase, particles experience considerably more

 $<sup>^{1}</sup>$  1 g = 9.8 m/s2.

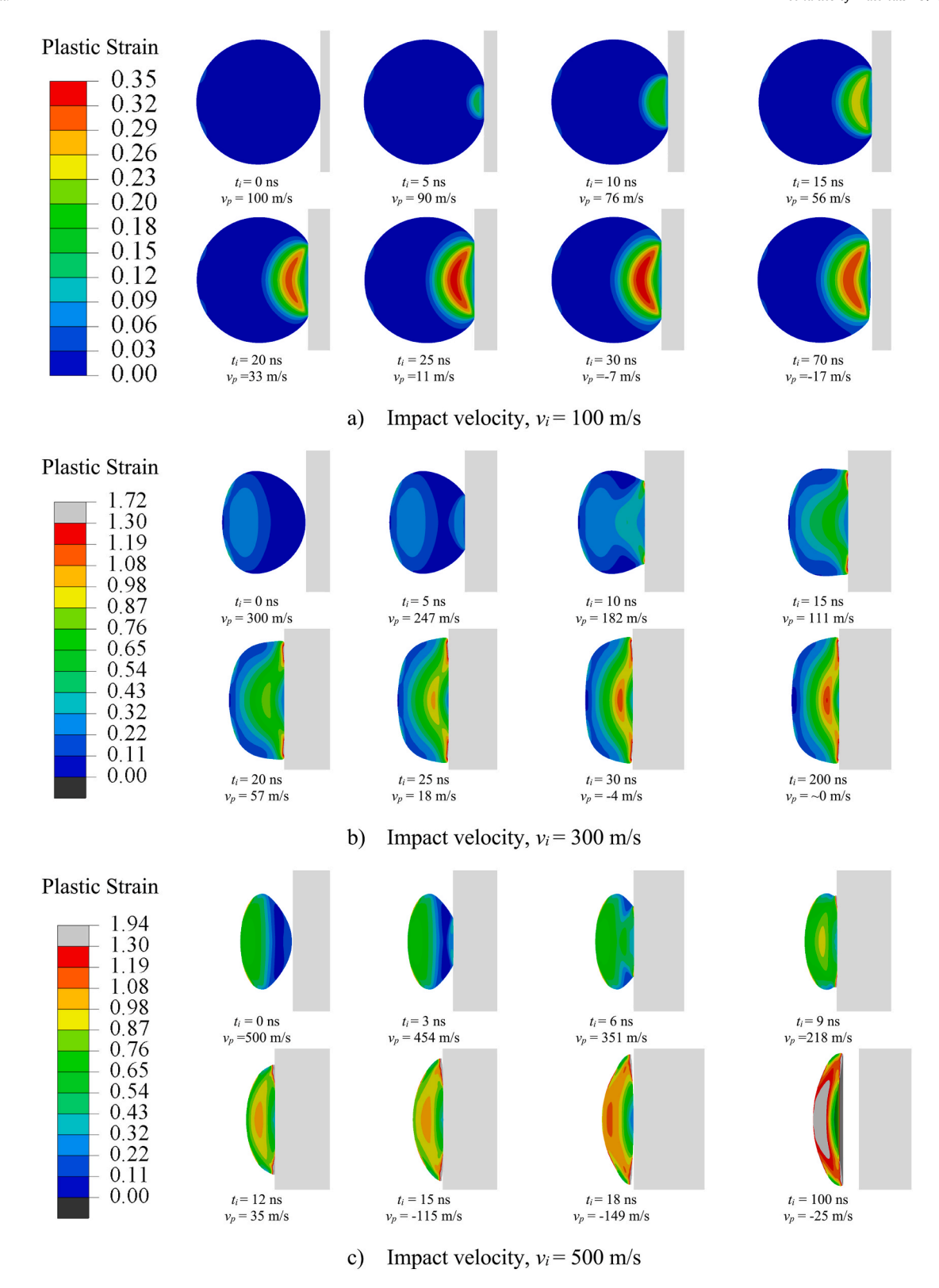


Fig. 16. Effective plastic strain evolution during impact of the particle for terminal velocity of a) 100 m/s b) 300 m/s c) 500 m/s.

deformation and additional plastic strain as compared to the acceleration phase. Maximum equivalent plastic strain values are 0.35, 1.72, and 1.94 for impact velocities of 100, 300, and 500 m/s, respectively. The particle gradually decelerates upon impact, and a rebound phase takes over. This process is dominated by the elastic strain energy stored in the system, as discussed by Yildirim et al. (2017). For  $v_i = 300$  m/s the

particle remains stuck on the substrate surface due to the cohesive interaction between the particle and the substrate (see Fig. 6b for these impact velocities). With increasing impact velocity, particle deformation becomes more severe and the lateral deformation of the particles increases. The diameter ( $D_c$ ) of the contact area is plotted as a function of impact velocity in Fig. 18. In regions-I and –II the contact diameter

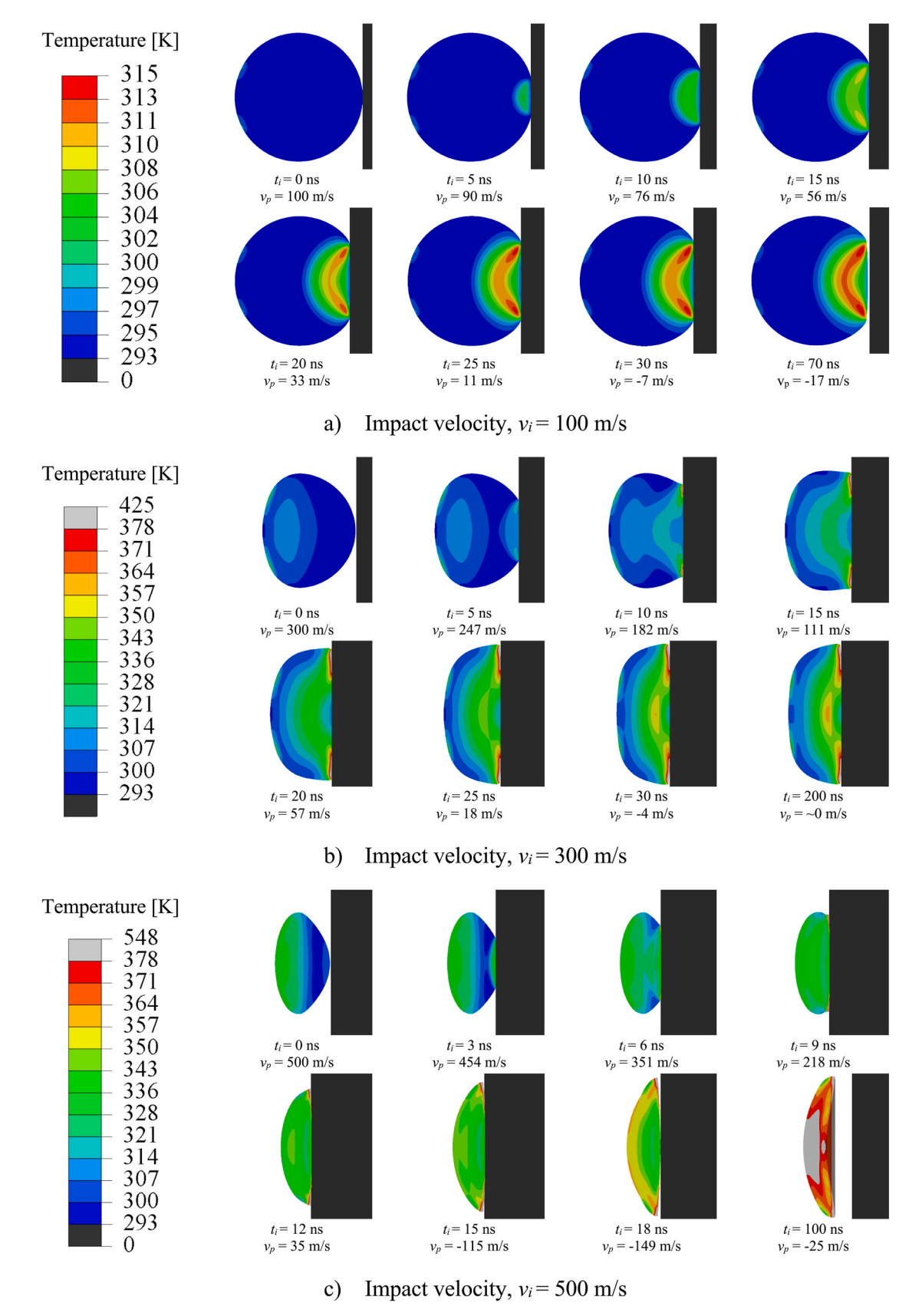
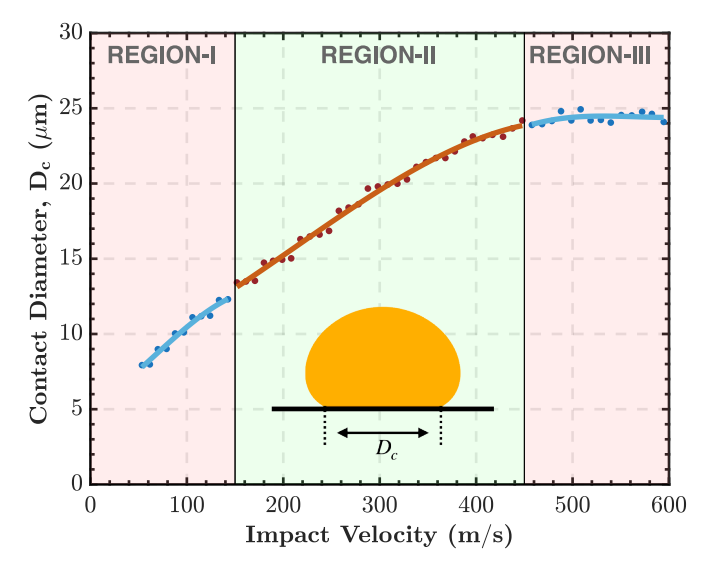


Fig. 17. Temperature evolution during impact of the particle for terminal velocity of a) 100 m/s b) 300 m/s c) 500 m/s.



**Fig. 18.** Contact diameter of the polymer particles as a function of impact velocity. The non-monotonic variation in the numerically calculated contact diameters is attributed to the finite element mesh size and is expected to diminish with mesh refinement.

increases with increasing impact velocity. Inreasing contact area provides increasing adhesive force on the particle. In region-III the particles can no longer spread laterally and the contact diameter is nearly constant. In this region, the rebound force which increases with increasing impact velocity, again defeats the adhesive forces and the particles rebound.

The average acceleration and velocity in the impact phase reveal rich dynamic interactions (Fig. 15b). The initial contact slows down the particle, but the elastic energy initiates a rebound wave, as described by Yildirim et al. (2017). For  $y_i = 300$  m/s, the rebound energy is smaller

than the cohesive energy, the particle remains on the surface, and the average particle velocity fluctuates and eventually settles down to zero after 250–300 ns. For  $\nu_i=100$ , and 500 m/s, particles rebound after complete delamination from the surface with non-zero rebound kinetic energies.

Particle deformation during the impact phase causes substantial plastic deformation (Fig. 16) and temperature rise (Fig. 17). In fact, the temperature rise of 22 K, 125 K, and 255 K in the particles for the three impact velocities (Fig. 17) are considerably higher than the temperature rise the particles experience in the acceleration phase. The two sources for temperature rise are plastic action in the particles and frictional dissipation in the interface. The CZM used in this work results in immediate bonding when the particle comes in contact with the substrate, independent of the conditions, e.g. contact pressure and temperature, in the interface. This may not be completely accurate in high velocity impacts during which the particle spreads significantly over the surface, and it becomes hard to rule out slip or stick-slip taking place in the interface prior to complete bonding. This behavior can not be captured with the current CZM, which rules out relative sliding and makes the frictional energy dissipation zero (Alfano and Sacco, 2006). Lack of sliding persists as long as the damage parameter D < 1. As a result, in our simulations the plastic energy dissipation dominates the temperature increase in the interface during the impact phase of the simulation. In fact, a comparison of the maximum temperature contours (Fig. 17) with maximum plastic strain contours (Fig. 16) shows a good correlation between the two variables since the plastic dissipation is the only source of temperature rise inside the particle. The total plastic dissipation in the particles in the impact phase is 9, 89, and 181 nJ for the three impact speeds, respectively (Fig. 15d).

Predictions of the particle temperatures at  $(t_i = )$  100 ns after the impact are plotted in Fig. 19 for a range of impact velocities (75–550 m/s). Temperature values that are predicted to be higher than the glass transition temperature (378 K) of polystyrene are plotted in grey. Highest temperatures are predicted at or near the contact interface where frictional and plastic dissipation is highest. The case of  $v_i = 550$ 

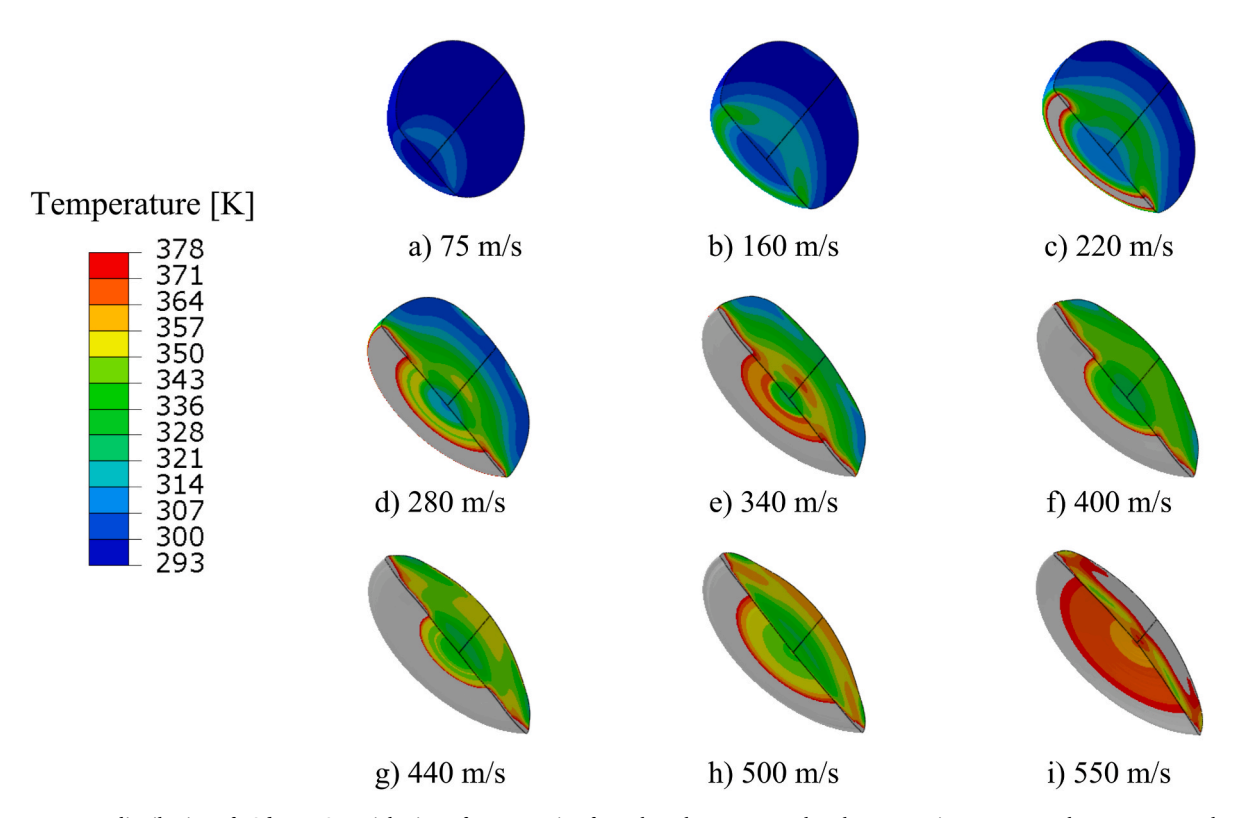


Fig. 19. Temperature distribution of PS-b-PDMS particles just after separation from the substrate. Note that the grey regions represent the temperature above  $T_g$  and impact velocity is reported under each particle.

m/s is an exception, where the top of the particle also shows very high temperatures due to plastic deformation alone. Given the observed temperature increases, it is reasonable to ask if the BCP will undergo a phase change from its glassy state to a more rubbery state. Note that the glass transition temperatures of the rubbery (PDMS) and the glassy (polystyrene) domains of this BCP are 148 K and 378 K, respectively. Thus PDMS is already above its  $T_g$  limit even at the room temperature and only the polystyrene-domain can experience the glass transition. The particle temperature is predicted to be below 378 K up to  $v_i = 210$ m/s and to increase near the contact interface with increasing impact velocities. Thus, according to these results, the polystrene-domain of the BCP will experience glass transition in a volume near the contact interface for  $v_i > 210$  m/s. In fact, the outer rim of the contact interface is where the highest surface temperatures are observed. Considering segmental reordering in BCPs depends on temperature, pressure, and rate of deformation (Roland et al., 2005; Bogoslovov et al., 2007; Kim et al., 2023), it is reasonable to state that segmental reordering is likely to occur in the volume near the contact interface where material temperatures exceed the  $T_g$  of the polystyrene-domain.

# 6. Summary and conclusions

Impact mechanics of a two-phase BCP (PS-b-PDMS) against a silicon wafer was investigated. Single particle impact experiments conducted at room temperature revealed that the particles bond to the substrate in the  $\sim\!140-\sim\!500$  m/s impact velocity window. Images of the particles in flight showed that they deform due to the nature of the acceleration mechanism in the  $\alpha$ -LIPIT test setup. A temperature and strain rate dependent constitutive model was developed and calibrated for this BCP. An interesting acceleration mechanism is revealed by simulations where the rapid expansion of the membrane of the  $\alpha$ -LIPIT system causes substantial plastic deformation in the particle during first 50 ns of their interaction. This interaction explains the deformations observed in the experiments, and it is unique to the  $\alpha$ -LIPIT test setup. Initial deformation in polymer-CS could also occur when the powder impacts the nozzle walls. Therefore, further investigation of this behavior is indicated.

Simulations of the impact phase show that the particles experience substantial plastic deformation and temperature rise during deceleration. In general, plastic dissipation and temperature rise increase with increasing impact velocity. A localized volume near contact interface experiences temperatures above  $T_g$  of the PS-domain. In this region, temperature rise is due to a combination of plastic and frictional energy dissipation mechanisms. While the thermal softening is captured effectively with the constitutive model introduced in this work, an appropriate constitutive model for  $T > T_g$  should be developed in future work.

Bonding in the polymer-particle/silicon-wafer interface was modeled by using a piecewise temperature and rate of separation dependent cohesive zone model with  $G_c = 9.3 \, \mathrm{J/m^2}$  at the low end of the bonding window and  $G_c = 48 \, \mathrm{J/m^2}$  at the high end. The change in the bonding energy is shown to depend on the temperature and the rate of separation. This work shows strong correlations between bonding and increases in critical fracture toughness, contact area and temperature that the particles experience with increasing impact velocity.

# **Funding**

This material is based upon work supported by the National Science Foundation under Grant No. 1760924. Any opinions, findings, and conclusions or recommendations expressed in this material are those of the author(s) and do not necessarily reflect the views of the National Science Foundation.

# **Author Credit Statement**

Salih Duran: Methodology, Validation, Formal analysis, Investigation, Writing – original draft, Visualization: Ara Kim: Methodology,

Validation, Formal analysis, Investigation, Writing – review & editing, Visualization: Jae-Hwang Lee: Conceptualization, Methodology, Writing – review & editing, Supervision, Project administration, Funding acquisition: Sinan Müftü; Conceptualization, Methodology, Formal analysis, Writing – review & editing, Supervision, Project administration, Funding acquisition

#### **Declaration of competing interest**

The authors declare that they have no known competing financial interests or personal relationships that could have appeared to influence the work reported in this paper.

## Data availability

Data will be made available on request.

#### References

- Al-Juaid, A.A., Othman, R., 2016. Modeling of the strain rate dependency of polycarbonate's yield stress: evaluation of four constitutive equations. J. Eng. 1–9. https://doi.org/10.1155/2016/6315421, 2016.
- Alfano, G., Sacco, E., 2006. Combining interface damage and friction in a cohesive-zone model. Int. J. Numer. Methods Eng. 68, 542–582. https://doi.org/10.1002/ nme.1728.
- Alhulaifi, A.S., Buck, G.A., Arbegast, W.J., 2012. Numerical and experimental investigation of cold spray gas dynamic effects for polymer coating. J. Therm. Spray Technol. 21, 852–862. https://doi.org/10.1007/s11666-012-9743-4.
- Anni, I.A., Kaminskyj, M.S., Uddin, K.Z., Bacha, T.W., Singh, N.K., Stanzione, J.F., Haas, F.M., Koohbor, B., 2023. Thermoplastic coating on fiber reinforced polymer composites by cold spray additive manufacturing. Mater. Today Commun. 35, 105650 https://doi.org/10.1016/j.mtcomm.2023.105650.
- Armstrong, R.W., Zerilli, F.J., 1994. Dislocation mechanics aspects of plastic instability and shear banding. Mech. Mater. 17, 319–327. https://doi.org/10.1016/0167-6636 (94)90069-8.
- Arruda, E.M., Boyce, M.C., 1993. A three-dimensional constitutive model for the large stretch behavior of rubber elastic materials. J. Mech. Phys. Solid. 41, 389–412. https://doi.org/10.1016/0022-5096(93)90013-6
- Banea, M.D., da Silva, L.F.M., Campilho, R.D.S.G., 2012. Effect of temperature on tensile strength and mode I fracture toughness of a high temperature epoxy adhesive. J. Adhes. Sci. Technol. 26, 939–953. https://doi.org/10.1163/156856111X593649.
- Barnett, B., 2012. Cold Spray Technology for DOD Applications. Bergström, J., 2022. PolyUMod User's Manual. PolymerFEM, LLC, Needham, MA, p. 7.
- Bergström, J.S., Boyce, M.C., 2000. Large strain time-dependent behavior of filled elastomers. Mech. Mater. 32, 627–644. https://doi.org/10.1016/S0167-6636(00)
- Blok, H., 1963. The flash temperature concept. Wear 6, 483–494. https://doi.org/ 10.1016/0043-1648(63)90283-7.
- Bogoslovov, R.B., Roland, C.M., Gamache, R.M., 2007. Impact-induced glass transition in elastomeric coatings. Appl. Phys. Lett. 90, 221910 https://doi.org/10.1063/
- Bortolussi, V., Figliuzzi, B., Willot, F., Faessel, M., Jeandin, M., 2020. Electrical conductivity of metal–polymer cold spray composite coatings onto carbon fiber-reinforced polymer. J. Therm. Spray Technol. 29, 642–656. https://doi.org/10.1007/s11666-020-00999-7.
- Bush, T.B., Khalkhali, Z., Champagne, V., Schmidt, D.P., Rothstein, J.P., 2017.
  Optimization of cold spray deposition of high-density polyethylene powders.
  J. Therm. Spray Technol. 26, 1548–1564. https://doi.org/10.1007/s11666-017-0627-5.
- Chakrabarty, R., Song, J., 2020. A modified Johnson-Cook material model with strain gradient plasticity consideration for numerical simulation of cold spray process. Surf. Coat. Technol. 397, 125981 https://doi.org/10.1016/j.surfcoat.2020.125981.
- Che, H., Vo, P., Yue, S., 2019. Investigation of cold spray on polymers by single particle impact experiments. J. Therm. Spray Technol. 28, 135–143. https://doi.org/ 10.1007/s11666-018-0801-4.
- Chen, Q., Alizadeh, A., Xie, W., Wang, X., Champagne, V., Gouldstone, A., Lee, J.-H., Müftü, S., 2018. High-strain-rate material behavior and adiabatic material instability in impact of micron-scale Al-6061 particles. J. Therm. Spray Technol. 27, 641–653. https://doi.org/10.1007/s11666-018-0712-4.
- Cho, H., Rinaldi, R.G., Boyce, M.C., 2013. Constitutive modeling of the rate-dependent resilient and dissipative large deformation behavior of a segmented copolymer polyurea. Soft Matter 9, 6319. https://doi.org/10.1039/c3sm27125k.
- Cho, H., Mayer, S., Pöselt, E., Susoff, M., P. J., Rutledge, G.C., Boyce, M.C., 2017. Deformation mechanisms of thermoplastic elastomers: stress-strain behavior and constitutive modeling. Polymer (Guildf) 128, 87–99. https://doi.org/10.1016/j.polymer.2017.08.065.
- Couque, H., Boulanger, R., Bornet, F., 2006. A modified Johnson-Cook model for strain rates ranging from 10  $^{-3}$  to 10  $^{5}$  s  $^{-1}$ . J. Phys. IV 134, 87–93. https://doi.org/10.1051/jp4:2006134015.

- Diehl, T., 2008a. On using a penalty-based cohesive-zone finite element approach, Part I: elastic solution benchmarks. Int. J. Adhesion Adhes. 28, 237–255. https://doi.org/ 10.1016/j.ijadhadh.2007.06.003.
- Diehl, T., 2008b. On using a penalty-based cohesive-zone finite element approach, Part II: inelastic peeling of an epoxy-bonded aluminum strip. Int. J. Adhesion Adhes. 28, 256–265. https://doi.org/10.1016/j.ijadhadh.2007.06.004.
- El-Qoubaa, Z., Othman, R., 2015. Characterization and Modeling of the Strain Rate Sensitivity of Polyetheretherketone's Compressive Yield Stress. Materials & Design, pp. 336–345. https://doi.org/10.1016/j.matdes.2014.10.080, 1980-2015.
- Evans, W.C., Dan, X., Houshmand, A., Mülftü, S., Ando, T., 2019. Microstructural characterization of aluminum 6061 splats cold spray deposited on aluminum 6061-T6 substrate. Metall. Mater. Trans. 50, 3937–3948. https://doi.org/10.1007/s11661-019-05303-z
- Feng, W., Xu, F., Li, Z., Zhang, C., 2023. Mode I fracture toughness of adhesively bonded composite joints under high loading rate conditions. J. Adhes. 99, 893–909. https:// doi.org/10.1080/00218464.2022.2061351.
- Flanagan, T.J., Bedard, B.A., Dongare, A.M., Brody, H.D., Nardi, A., Champagne, V.K., Aindow, M., Lee, S.-W., 2019. Mechanical properties of supersonic-impacted Al6061 powder particles. Scripta Mater. 171, 52–56. https://doi.org/10.1016/j. scriptart.2019.06.024
- Ganesan, A., Yamada, M., Fukumoto, M., 2013. Cold spray coating deposition mechanism on the thermoplastic and thermosetting polymer substrates. J. Therm. Spray Technol. 22, 1275–1282. https://doi.org/10.1007/s11666-013-9984-x.
- Gao, C.Y., Zhang, L.C., 2012. Constitutive modelling of plasticity of fcc metals under extremely high strain rates. Int. J. Plast. 32–33, 121–133. https://doi.org/10.1016/j. iiplas.2011.12.001.
- Grujicic, M., Saylor, J.R., Beasley, D.E., DeRosset, W.S., Helfritch, D., 2003. Computational analysis of the interfacial bonding between feed-powder particles and the substrate in the cold-gas dynamic-spray process. Appl. Surf. Sci. 219, 211–227. https://doi.org/10.1016/S0169-4332(03)00643-3.
- Grujicic, M., Snipes, J.S., Ramaswami, S., Yavari, R., Runt, J., Tarter, J., Dillon, G., 2013. Coarse-grained molecular-level analysis of polyurea properties and shock-mitigation potential. J. Mater. Eng. Perform. 22, 1964–1981. https://doi.org/10.1007/s11665-013-0485-3
- Hassani-Gangaraj, M., Veysset, D., Nelson, K.A., Schuh, C.A., 2018. In-situ observations of single micro-particle impact bonding. Scripta Mater. 145, 9–13. https://doi.org/ 10.1016/j.scriptamat.2017.09.042.
- Hyon, J., Lawal, O., Fried, O., Thevamaran, R., Yazdi, S., Zhou, M., Veysset, D., Kooi, S. E., Jiao, Y., Hsiao, M.-S., Streit, J., Vaia, R.A., Thomas, E.L., 2018. Extreme energy absorption in glassy polymer thin films by supersonic micro-projectile impact. Mater. Today 21, 817–824. https://doi.org/10.1016/j.mattod.2018.07.014.
- J G, R., 1983. A constitutive model and data for materials subjected to large strains, high strain rates, and high temperatures. Proc. 7th Inf. Sympo. Ballistics. 541–547. https: //cir.nii.ac.jp/crid/1570854176356644864.bib?lang=en. (Accessed 26 March 2023).
- Jung, Y.S., Ross, C.A., 2007. Orientation-controlled self-assembled nanolithography using a Polystyrene–Polydimethylsiloxane block copolymer. Nano Lett. 7, 2046–2050. https://doi.org/10.1021/nl0709241.
- Kausar, A., 2018. Polymer coating technology for high performance applications: fundamentals and advances. J. Macromol. Sci., Part A. 55, 440–448. https://doi.org/ 10.1080/10601325.2018.1453266.
- Kendall, M.J., Froud, R.F., Siviour, C.R., 2014. Novel temperature measurement method & thermodynamic investigations of amorphous polymers during high rate deformation. Polymer (Guildf) 55, 2514–2522. https://doi.org/10.1016/j. polymer 2014 03 058
- Khalkhali, Z., Rothstein, J.P., 2020. Characterization of the cold spray deposition of a wide variety of polymeric powders. Surf. Coat. Technol. 383, 125251 https://doi. org/10.1016/j.surfcoat.2019.125251
- Khalkhali, Z., Xie, W., Champagne, V.K., Lee, J.-H., Rothstein, J.P., 2018. A comparison of cold spray technique to single particle micro-ballistic impacts for the deposition of polymer particles on polymer substrates. Surf. Coat. Technol. 351, 99–107. https:// doi.org/10.1016/j.surfcoat.2018.07.053.
- Kim, A., Duran, S., Avgeropoulos, A., Müftü, S., Lee, J.-H., 2023. Extreme plasticity, adhesion, and nanostructural changes of diblock copolymer microparticles in cold spray additive manufacturing. ACS Appl. Polym. Mater. https://doi.org/10.1021/psepp. 201025
- Lee, J.-H., Veysset, D., Singer, J.P., Retsch, M., Saini, G., Pezeril, T., Nelson, K.A., Thomas, E.L., 2012. High strain rate deformation of layered nanocomposites. Nat. Commun. https://doi.org/10.1038/ncomms2166.
- Lesuer, D.R., Kay, G.J., LeBlanc, M.M., 2001. Modeling large-strain, high-rate deformation in metals. In: United States. https://www.osti.gov/biblio/15005327.
- Lin, E., Chen, Q., Ozdemir, O.C., Champagne, V.K., Müftü, S., 2019. Effects of interface bonding on the residual stresses in cold-sprayed Al-6061: a numerical investigation. J. Therm. Spray Technol. 28, 472–483. https://doi.org/10.1007/s11666-019-00827-7.
- Manes, A., Peroni, L., Scapin, M., Giglio, M., 2011. Analysis of strain rate behavior of an Al 6061 T6 alloy. Procedia Eng. 10, 3477–3482. https://doi.org/10.1016/j. proeng.2011.04.573.
- Manes, A., Lumassi, D., Giudici, L., Giglio, M., 2013. An experimental–numerical investigation on aluminium tubes subjected to ballistic impact with soft core 7.62 ball projectiles. Thin-Walled Struct. 73, 68–80. https://doi.org/10.1016/j. tws.2013.07.015.
- Marzi, S., Hesebeck, O., Brede, M., Kleiner, F., 2009. A rate-dependent cohesive zone model for adhesively bonded joints loaded in mode I. J. Adhes. Sci. Technol. 23, 881–898. https://doi.org/10.1163/156856109X411238.

- Moridi, A., Hassani-Gangaraj, S.M., Guagliano, M., Dao, M., 2014. Cold spray coating: review of material systems and future perspectives. Surf. Eng. 30, 369–395. https://doi.org/10.1179/1743294414Y.0000000270.
- Muthulingam, J., Padmanaban, A.G., Singh, N.K., Bacha, T.W., Stanzione, J.F., Haas, F. M., Jha, R., Lee, J.-H., Koohbor, B., 2023. Molecular weight controls interactions between plastic deformation and fracture in cold spray of glassy polymers. ACS Omega 8, 3956–3970. https://doi.org/10.1021/acsomega.2c06617.
- Needleman, A., 1990. An analysis of tensile decohesion along an interface. J. Mech. Phys. Solid. 38, 289–324. https://doi.org/10.1016/0022-5096(90)90001-K.
- Othman, R., 2015. A modified eyring equation for modeling yield and flow stresses of metals at strain rates ranging from  $10^{-5}$  to  $5\times10^{4\,s}-1$ . Adv. Mater. Sci. Eng. 1–6. https://doi.org/10.1155/2015/539625.
- Ozdemir, O.C., Chen, Q., Muftu, S., Champagne, V.K., 2019. Modeling the continuous heat generation in the cold spray coating process. J. Therm. Spray Technol. 28, 108–123. https://doi.org/10.1007/s11666-018-0794-z.
- Ozdemir, O.C., Schwartz, P., Muftu, S., Thompson, F.C., Crawford, G.A., Nardi, A.T., Champagne, V.K., Widener, C.A., 2021. High rate deposition in cold spray. J. Therm. Spray Technol. 30, 344–357. https://doi.org/10.1007/s11666-020-01135-1.
- Papyrin, A., Kosarev, V., Klinkov, S., Alkimov, A., Fomin, V., 2007. Discovery of the cold spray phenomenon and its basic features. In: Cold Spray Technology, pp. 1–32. https://doi.org/10.1016/B978-008045155-8/50001-6. Elsevier.
- Preston, D.L., Tonks, D.L., Wallace, D.C., 2003. Model of plastic deformation for extreme loading conditions. J. Appl. Phys. 93, 211–220. https://doi.org/10.1063/ 1.1524706.
- Ravi, K., Ichikawa, Y., Deplancke, T., Ogawa, K., Lame, O., Cavaille, J.-Y., 2015. Development of ultra-high molecular weight polyethylene (UHMWPE) coating by cold spray technique. J. Therm. Spray Technol. 24, 1015–1025. https://doi.org/ 10.1007/s11666-015-0276-5.
- Rokni, M.R., Feng, P., Widener, C.A., Nutt, S.R., 2019. Depositing Al-based metallic coatings onto polymer substrates by cold spray. J. Therm. Spray Technol. 28, 1699–1708. https://doi.org/10.1007/s11666-019-00911-y.
- Roland, C.M., Hensel-Bielowka, S., Paluch, M., Casalini, R., 2005. Supercooled dynamics of glass-forming liquids and polymers under hydrostatic pressure. Rep. Prog. Phys. 68, 1405–1478. https://doi.org/10.1088/0034-4885/68/6/R03.
- Sabard, A., Hussain, T., 2019. Inter-particle bonding in cold spray deposition of a gasatomised and a solution heat-treated Al 6061 powder. J. Mater. Sci. 54, 12061–12078. https://doi.org/10.1007/s10853-019-03736-w.
- Sarva, S.S., Deschanel, S., Boyce, M.C., Chen, W., 2007. Stress-strain behavior of a polyurea and a polyurethane from low to high strain rates. Polymer (Guildf) 48, 2208–2213. https://doi.org/10.1016/j.polymer.2007.02.058.
- Schmidt, T., Assadi, H., Gärtner, F., Richter, H., Stoltenhoff, T., Kreye, H., Klassen, T., 2009. From particle acceleration to impact and bonding in cold spraying. J. Therm. Spray Technol. 18, 794. https://doi.org/10.1007/s11666-009-9357-7.
- Schreiber, J.M., Smid, I., Eden, T.J., Koudela, K., Cote, D., Champagne, V., 2021. Cold spray particle impact simulation using the Preston-Tonks-Wallace plasticity model. Finite Elem. Anal. Des. 191, 103557 https://doi.org/10.1016/j.finel.2021.103557.
- Shah, S., Lee, J., Rothstein, J.P., 2017. Numerical simulations of the high-velocity impact of a single polymer particle during cold-spray deposition. J. Therm. Spray Technol. 26, 970–984. https://doi.org/10.1007/s11666-017-0557-2.
- Shao, G., Zhu, S., Wang, Y., Zhao, Q., 2017. An internal state variable thermodynamic model for determining the Taylor-Quinney coefficient of glassy polymers. Int. J. Mech. Sci. 126, 261–269. https://doi.org/10.1016/j.ijmecsci.2017.03.026.
- Smith, M.F., 2007. Comparing cold spray with thermal spray coating technologies. In: Champagne, V.K. (Ed.), The Cold Spray Materials Deposition Process. Elsevier, pp. 43–61. https://doi.org/10.1533/9781845693787.1.43.
- Stoltenhoff, T., Kreye, H., Richter, H.J., 2002. An analysis of the cold spray process and its coatings. J. Therm. Spray Technol. 11, 542–550. https://doi.org/10.1361/ 105996302770348682
- Sun, Y., Wu, Y.-C.M., Veysset, D., Kooi, S.E., Hu, W., Swager, T.M., Nelson, K.A., Hsieh, A.J., 2019. Molecular dependencies of dynamic stiffening and strengthening through high strain rate microparticle impact of polyurethane and polyurea elastomers. Appl. Phys. Lett. 115, 093701 https://doi.org/10.1063/1.5111964.
- Tuazon, B.J., Bae, K.-O., Lee, S.-H., Shin, H.-S., 2014. Integration of a new data acquisition/processing scheme in SHPB test and characterization of the dynamic material properties of high-strength steels using the optional form of Johnson-Cook model. J. Mech. Sci. Technol. 28, 3561–3568. https://doi.org/10.1007/s12206-014-0817-8
- Van Steenkiste, T.H., Smith, J.R., Teets, R.E., Moleski, J.J., Gorkiewicz, D.W., Tison, R.P., Marantz, D.R., Kowalsky, K.A., Riggs, W.L., Zajchowski, P.H., Pilsner, B., McCune, R. C., Barnett, K.J., 1999. Kinetic spray coatings. Surf. Coat. Technol. 111, 62–71. https://doi.org/10.1016/S0257-8972(98)00709-9.
- Veyssef, D., Hsieh, A.J., Kooi, S.E., Nelson, K.A., 2017. Molecular influence in high-strain-rate microparticle impact response of poly(urethane urea) elastomers. Polymer (Guildf) 123, 30–38. https://doi.org/10.1016/j.polymer.2017.06.071.
- Voyiadjis, G.Z., Abed, F.H., 2005. Microstructural based models for bcc and fcc metals with temperature and strain rate dependency. Mech. Mater. 37, 355–378. https://doi.org/10.1016/j.mechmat.2004.02.003.
- Wu, Y.-C.M., Hu, W., Sun, Y., Veysset, D., Kooi, S.E., Nelson, K.A., Swager, T.M., Hsieh, A.J., 2019. Unraveling the high strain-rate dynamic stiffening in select model polyurethanes – the role of intermolecular hydrogen bonding. Polymer (Guildf) 168, 218–227. https://doi.org/10.1016/j.polymer.2019.02.038.
- Xie, W., Alizadeh-Dehkharghani, A., Chen, Q., Champagne, V.K., Wang, X., Nardi, A.T., Kooi, S., Müftü, S., Lee, J.-H., 2017. Dynamics and extreme plasticity of metallic microparticles in supersonic collisions. Sci. Rep. 7, 5073. https://doi.org/10.1038/ s41598-017-05104-7.

- Xu, Y., Hutchings, I.M., 2006. Cold spray deposition of thermoplastic powder. Surf. Coat. Technol. 201, 3044–3050. https://doi.org/10.1016/j.surfcoat.2006.06.016.
  Yildirim, B., Fukanuma, H., Ando, T., Gouldstone, A., Müftü, S., 2015. A numerical investigation into cold spray bonding processes. J. Tribol. 137 https://doi.org/10.1115/1.4028471.
- Yildirim, B., Yang, H., Gouldstone, A., Müftü, S., 2017. Rebound mechanics of micrometre-scale, spherical particles in high-velocity impacts. Proc. R. Soc. A 473, 20160936. https://doi.org/10.1098/rspa.2016.0936.